



1 Improving the representation of HONO chemistry in 2 CMAQ and examining its impact on haze over China

3 Shuping Zhang,^{1,2,3} Golam Sarwar,⁴ Jia Xing,² Biwu Chu,^{1,3,5} Chaoyang Xue,^{1,3}
4 Arunachalam Sarav,⁶ Dian Ding,² Haotian Zheng,² Yujing Mu,^{1,3,5} Fengkui Duan,²
5 Tao Ma,² Hong He^{1,3,5}

6 ¹State Key Joint Laboratory of Environment Simulation and Pollution Control, Research Center for
7 Eco-Environmental Sciences, Chinese Academy of Sciences, Beijing 100085, China

8 ²State Key Joint Laboratory of Environment Simulation and Pollution Control, School of Environment,
9 Tsinghua University, Beijing 100084, China

10 ³University of Chinese Academy of Sciences, Beijing 100049, China

11 ⁴Center for Environmental Measurement and Modeling, U.S. Environmental Protection Agency, 109
12 T.W. Alexander Drive, Research Triangle Park, NC, 27711, USA

13 ⁵Center for Excellence in Regional Atmospheric Environment, Institute of Urban Environment,
14 Chinese Academy of Sciences, Xiamen 361021, China

15 ⁶Institute for the Environment, The University of North Carolina at Chapel Hill, 100 Eurpoa Drive,
16 Chapel Hill, NC 27514, USA

17 *Correspondence to:* Golam Sarwar(Sarwar.Golam@epa.gov), Jia Xing(xingjia@tsinghua.edu.cn), Hong
18 He(honghe@rcees.ac.cn)

19 **Abstract.** We compare Community Multiscale Air Quality (CMAQ) model predictions with measured
20 nitrous acid (HONO) concentrations in Beijing, China for December 2015. The model with the existing
21 HONO chemistry in CMAQ severely under-estimates the observed HONO concentrations with a
22 normalized mean bias of -97%. We revise the HONO chemistry in the model by implementing six
23 additional heterogeneous reactions in the model: reaction of nitrogen dioxide (NO₂) on ground surfaces,
24 reaction of NO₂ on aerosol surfaces, reaction of NO₂ on soot surfaces, photolysis of aerosol nitrate, nitric
25 acid displacement reaction, and hydrochloric acid displacement reaction. The model with the revised
26 chemistry substantially increases HONO predictions and improves the comparison with observed data
27 with a normalized mean bias of -5%. The photolysis of HONO enhances day-time hydroxyl radical by
28 almost a factor of two. The enhanced hydroxyl radical concentrations compare favorably with observed
29 data and produce additional sulfate via the reaction with sulfur dioxide, aerosol nitrate via the reaction
30 with nitrogen dioxide, and secondary organic aerosols via the reactions with volatile organic compounds.
31 The additional sulfate stemming from revised HONO chemistry improves the comparison with observed
32 concentration; however, it does not close the gap between model prediction and the observation during
33 polluted days.

34 1 Introduction

35 China has been suffering from haze pollution (Lelieveld et al., 2015) in which secondary particles
36 contribute more than 70% to the haze formation (Guo et al., 2014; Huang et al., 2014; Quan et al., 2014;
37 Zheng et al., 2015). However, the mechanism for the formation of high levels of secondary particles is



38 not yet clearly understood and most current air quality models tend to under-estimate particle
39 concentrations compared with observed data in China. Several secondary particle formation pathways
40 have been proposed, such as ①sulfate (SO_4^{2-}) formation via the heterogeneous oxidation of sulfur
41 dioxide (SO_2) promoted by hydrogen peroxide (H_2O_2) and/or ②nitrogen dioxide (NO_2) on mineral
42 dust (He et al., 2014; Huang et al., 2015; Ye et al., 2018), ③aqueous-phase oxidation of SO_2 promoted
43 by NO_2 in particle-bound water film (Wang et al., 2016; Li et al., 2017), ④aqueous-phase oxidation of
44 SO_2 by nitrous acid (HONO) produced from the photolysis of aerosol nitrate (NO_3^-) in particle-bound
45 water (Wang et al., 2016; Li et al., 2017), and ⑤ NO_3^- formation via efficient hydrolysis of dinitrogen
46 pentoxide (N_2O_5) on aerosol surfaces (Wang et al., 2017; Kulmala, 2018). However, the gap between
47 the model predictions and observed SO_4^{2-} is persistent and still large (Zhang et al., 2019c).

48
49 Previous studies suggested that the underestimation of atmospheric oxidation capacity during haze
50 limited the formation of secondary particles (Sun et al., 2013; Gen et al., 2019; Tsona and Du, 2019).
51 As a hydroxyl radical (OH) source, HONO plays an important role in the oxidation of precursors (Stutz
52 et al., 2002; Kleffmann et al., 2005). However, the large underestimation of HONO (up to the ppb level)
53 is prevalent during haze simulations around the world (Li et al., 2012; Fu et al., 2019; Zhang et al.,
54 2019d). Moreover, HONO underestimation is reported to be highly related to the formation of fine
55 particulate matter ($\text{PM}_{2.5}$) (Wang et al., 2015; Xue et al., 2020), particularly for secondary $\text{PM}_{2.5}$.
56 Compared with summer, HONO concentrations in winter tend to be high when secondary particle
57 underestimation occurs (Li et al., 2018a; Zhang et al., 2019b). The underestimation of HONO may
58 partly explain the phenomenon of insufficient oxidant for the formation of secondary particles during
59 the winter haze (Li et al., 2018b; Li et al., 2018c).

60
61 Sarwar et al. (2008) compared the CMAQ predictions with HONO concentrations measured in
62 Philadelphia, PA, USA, during a summer month (July 2001) and reported that the model with only
63 gas-phase chemistry seriously under-estimates observed concentrations. They implemented HONO
64 emissions from motor vehicles, the heterogeneous reaction on the ground and aerosol surfaces, and the
65 photolysis of nitric acid (HNO_3) deposited on environmental surfaces, which improved predicted
66 HONO concentrations; however, the underprediction persisted. The model with the revised chemistry
67 enhanced OH and ozone (O_3) concentrations. Li et al. (2010) examined the impact of HONO chemistry
68 in Mexico City using the Weather Research and Forecasting model, coupled with chemistry
69 (WRF-CHEM). They added five different HONO reactions: ① the gas-phase reaction between NO
70 (nitric oxide) and OH, ②the heterogeneous reaction of NO_2 on the aerosol surfaces, ③the
71 heterogeneous reaction of NO_2 on the ground surfaces, ④the heterogeneous reaction of NO_2 with
72 semi-volatile organics, and ⑤ NO_2 reaction with freshly emitted soot. The model successfully
73 reproduced observed HONO concentrations in Mexico City during March 2006. The model with the
74 HONO chemistry increased OH, HO_2 (hydroperoxyl radical), O_3 , secondary organic aerosols (SOA),
75 NO_3^- , and ammonium (NH_4^+) and improved the comparison with observed data. The enhancements
76 were particularly high in the morning. However, the impact on SO_4^{2-} was negligible. Czader et al. (2012)
77 compared CMAQv5.3 predictions with HONO measured during August and September 2006 in
78 Houston, TX, USA, and also reported that the model with gas-phase alone was not sufficient to explain
79 the observed data and predicted concentrations. They added HONO emissions, NO_2 hydrolysis, active
80 NO_2 chemistry, and conversion of NO_2 into HONO on organic materials covered surfaces, which
81 improved model performance for HONO and, subsequently, increased OH and O_3 concentrations.



82

83 Fu et al. (2019) studied a 5-day episode (January 4-8, 2017) in the Pearl River Delta of China during
84 which high levels of particles, O₃, and HONO concentrations were measured. They implemented four
85 additional reactions for HONO production into the model: ① relative humidity-dependent
86 heterogeneous reaction of NO₂, ② light-dependent heterogeneous reaction of NO₂, ③ photolysis of
87 NO₃⁻, and ④ photolysis of HNO₃ on surfaces. The model with the additional chemistry successfully
88 reproduced measured HONO concentrations which subsequently enhanced and improved O₃ and PM_{2.5}
89 predictions. Xing et al. (2019) examined the impact of HONO chemistry on SOA in the
90 Beijing-Tianjin-Hebei area (BTH) of China using the WRF-CHEM model during January 9-26, 2014.
91 They employed the homogeneous and heterogeneous HONO chemistry of Li et al. (2010) and reported
92 that the HONO chemistry could increase the average SOA concentration by ~46%. Zhang et al. (2019a)
93 employed the WRF-CHEM model to examine the impact of HONO chemistry on OH, HO₂, and SOA
94 concentrations in the BTH region during a winter haze period (November 29–Dec. 3, 2017). They
95 employed six HONO sources in the model: ① traffic emissions, ② soil emissions, ③ biomass
96 burning emissions, ④ indoor emissions, ⑤ heterogeneous reaction on aerosol surfaces, and ⑥
97 heterogeneous reaction on ground surfaces. The model reproduced observed HONO concentrations and
98 substantially elevated OH, HO₂, and SOA concentrations.

99

100 In this study, we employ the Community Multiscale Air Quality (CMAQ) model to simulate and
101 compare HONO predictions with observed data from the field campaign in Beijing. The field campaign
102 was conducted during December 7-22, 2015, in Beijing, China, during which high concentrations of
103 HONO and aerosols were measured.

104 2 Methodology

105 2.1 Modeling framework and homogeneous HONO chemistry

106 The Community Multiscale Air Quality (CMAQv5.3) (USEPA, 2019) (<https://www.epa.gov/cmaq>) was
107 used widely in this study. CMAQv5.3 includes the representation of important atmospheric processes
108 and has been used widely in air quality studies in many countries, including China (Byun and Schere,
109 2006; Sarwar et al., 2008; Xing et al., 2015). The modeling domain, which covered China and
110 consisted of 182 × 232 horizontal grid-cells with a 27 × 27 km horizontal resolution and 14 vertical
111 layers encompassing surface to 100 hPa. The first layer height of the model was about 36 m. The static
112 initial and boundary conditions from CMAQv5.3 were used for the study. A 22-day model spin-up
113 period was used to minimize the effect of initial conditions on model predictions. The Carbon Bond 6
114 (version 3, CB6r3) (Emery et al., 2015) chemical mechanism that contain six homogeneous reactions
115 related to HONO (Table 1) was used without any modification. CMAQv5.3 contains a treatment of
116 heterogeneous conversion of NO₂ at aerosol and ground surfaces (Sarwar et al., 2008), in which uptake
117 coefficient at aerosol surfaces and aera density of ground surfaces were revised in this study (Section
118 2.2). CMAQv5.3 accounts for HONO emissions from motor vehicles as 0.008 × NO_x emissions which
119 were kept the same (NO_x = oxides of nitrogen, NO+NO₂). Photolysis rates (min⁻¹) in CMAQv5.3
120 (J-values) are computed for photo dissociation reactions by Eq. (1). Absorption cross-section and
121 quantum yield data suggested by the International Union of Pure and Applied Chemistry (IUPAC) are
122 used for calculating photolysis rates of HONO (Table 1)



123 (<http://iupac.pole-ether.fr/htdocs/datasheets/pdf>). Absorption cross-section and quantum yield data
 124 suggested by the IUPAC for NTR (organic nitrate) are used for calculating photolysis rates of CRON
 125 (nitro-cresol) (Table 1) (<http://iupac.pole-ether.fr/htdocs/datasheets/pdf>).
 126

$$127 \quad J_i = \int_{\lambda_1}^{\lambda_2} F(\lambda) \sigma_i(\lambda) \phi_i(\lambda) d\lambda \quad (1)$$

128 Note: $F(\lambda)$ is the actinic flux ($\text{photons cm}^{-2} \text{ min}^{-1} \text{ nm}^{-1}$), $\sigma_i(\lambda)$ the absorption cross section for the
 129 molecule undergoing photo dissociation ($\text{cm}^2 \text{ molecule}^{-1}$), $\phi_i(\lambda)$ the quantum yield of the photolysis
 130 reaction ($\text{molecules photon}^{-1}$), and λ the wavelength (nm).
 131

132 We also instrumented the model with the Integrated Reaction Rate (IRR) option, which enabled
 133 estimating the contribution of each reaction to the predicted HONO concentrations (Czader et al.,
 134 2013). The Sulfur Tracking Model in CMAQv5.3 was used to quantitatively calculate the contribution
 135 of each reaction to predicted SO_4^{2-} concentration (Mathur et al., 2008).
 136

137 **Table 1 Gas-phase chemical reactions related to HONO in CB6r3**

Reaction Number	Reaction	Reaction Rate Constant (k)
1	$\text{NO} + \text{OH} = \text{HONO}$	$k = \left\{ \frac{k_0 [M]}{(1 + k_0 [M]/k_1)} \right\} 0.81 \left\{ 1 + \left[\log_{10} \left(\frac{k_0 [M]}{k_1} \right) / 0.87 \right]^2 \right\}^{-1}$ $k_0 = 7.4 \times 10^{-31} \left(\frac{T}{300} \right)^{-2.4}$ $k_1 = 3.3 \times 10^{-11} \left(\frac{T}{300} \right)^{-0.3}$
2	$\text{NO} + \text{NO}_2 + \text{H}_2\text{O} = 2.0 \times \text{HONO}$	$k = 5.0 \times 10^{-40}$
3	$\text{HONO} + \text{HONO} = \text{NO} + \text{NO}_2$	$k = 1.0 \times 10^{-20}$
4	$\text{HONO} = \text{NO} + \text{OH}$	J_{HONO}
5	$\text{HONO} + \text{OH} = \text{NO}_2$	$k = 2.5 \times 10^{-12} e^{(260/T)}$
6	$\text{CRON} = \text{HONO} + \text{HO}_2 + \text{FORM} + \text{OPEN}$	J_{NTR}

138 Note: NO = nitric oxide, NO_2 = nitrogen dioxide, OH = hydroxyl radical, HO_2 = hydroperoxy radical,
 139 H_2O = water vapor, HONO = nitrous acid, CRON = nitro cresol; FORM = formaldehyde, OPEN =
 140 aromatic ring open product, [M] = total pressure (molecules/cm^3), T = air temperature (K), and k = rate
 141 constant. First-order rate constants are in units of s^{-1} , second-order rate constants are in units of cm^3
 142 $\text{molecule}^{-1} \text{ s}^{-1}$, third-order constants are in units of $\text{cm}^6 \text{ molecule}^{-2} \text{ s}^{-1}$. CMAQv5.3 converts
 143 cm-molecule-s units into ppm-min units before solving the system of ordinary differential equations for
 144 chemistry. J_{HONO} = photolysis of HONO, and J_{NTR} = photolysis of NTR (organic nitrate).
 145



146

147 2.2 Heterogeneous HONO chemistry

148 The understanding of heterogeneous HONO chemical reactions and parameter method is evolving.
149 Investigators have proposed hydrolysis of NO_2 on the humid aerosol surfaces, heterogeneous
150 conversion of NO_2 on ground surfaces, photolysis of NO_3^- , catalytical formation on soot particles and
151 acid displacement process in the atmosphere during the past several years (Stemmler et al., 2006; Liu et
152 al., 2014; Karamchandani et al., 2015; VandenBoer et al., 2015; Tong et al., 2016; Ye et al., 2016; Ye et
153 al., 2017; Lu et al., 2018; Xu et al., 2018b; Gen et al., 2019; Zhang et al., 2019d). Xue et al. (2020) and
154 Liu et al. (2019) recently measured summertime atmospheric HONO concentrations in a rural area in
155 China and performed simulations using a box model with updated chemical reactions for HONO
156 production published in the literature. They reported that the simulations generally reproduced
157 observed HONO concentrations using the updated HONO chemical reactions. However, the box model
158 did not consider horizontal and vertical transportation, limiting the impact of HONO formation on air
159 quality. We implement these updated chemical reactions into a three-dimensional (3D) air quality
160 model, CMAQv5.3, to examine their impacts on air quality.

161

162 Hydrolysis processes on the humid aerosol surfaces is an important HONO-producing reaction in the
163 atmosphere (An et al., 2012; Cui et al., 2018). And we use the uptake coefficient (Table 2) employed by
164 Liu et al. (2019) at night-time (Reaction 7a). The reaction on aerosols can be enhanced by light (Zhang
165 et al., 2019b); thus, we use a radiation-dependent uptake coefficient during day-time (Reaction 7b). We
166 use CMAQv5.3-calculated aerosol surface area-to-volume ratio (S/V_a) to calculate rate constant for the
167 reaction on aerosol surfaces. Heterogeneous conversion of NO_2 on ground surfaces also has been
168 studied intensively in the laboratory and field (Li et al., 2018a). Vertical night-time profile
169 measurements suggest that heterogeneous HONO formation on the ground is the dominant reaction;
170 thus, we also use this reaction. Similar to the heterogeneous reaction on aerosol surfaces, we employ an
171 uptake coefficient used by Liu et al. (2019) for the reaction at night (Reaction 8a) and a
172 radiation-dependent uptake coefficient during day-time (Reaction 8b). Following the suggestions of Li
173 et al., (2019) and Liu et al., (2019), we use a value of $1.7/H$ (H is the model's first-layer height) for
174 surface area-to-volume ratio of ground (S/V_g) to calculate the rate constant for the reaction on ground
175 surfaces.

176

177 Ye et al. (2016) proposed that the photolysis of NO_3^- can lead to HONO production in the atmosphere
178 and reported that its photolysis rates can be several hundred times faster than the photolysis rates of
179 HNO_3 . Bao et al. (2018) also reported similar photolysis rates of NO_3^- . Fu et al. (2019) used this high
180 photolysis rate in their study to examine the winter-time HONO production in Hong Kong. However,
181 Romer et al. (2018) reported that such high photolysis rates of NO_3^- are not consistent with observed
182 data over the Yellow Sea and should not be used in air quality models. They suggested that the
183 photolysis rates of NO_3^- in air quality models should be 1 to 30 times the photolysis rate of HNO_3 . For
184 photolysis of NO_3^- , we use a photolysis rate of 30 times the photolysis rate of HNO_3 (Reaction 9).

185

186 HONO formation on soot particles can be catalytically enhanced in the presence of artificial solar
187 radiation and lead to persistent reactivity of soot over long periods (Monge et al., 2010). The surface of
188 soot particles as a heterogeneous conversion media has been reported by several studies (Monge et al.,



189 2010; Liu et al., 2014; Spataro and Ianniello, 2014; Cui et al., 2018). The reported heterogeneous
 190 uptake coefficient on soot ranges from 10^{-8} to 10^{-6} , with HONO yields ranging between 50% and 100%
 191 (Spataro et al., 2013). This heterogeneous soot photochemistry potentially may contribute to day-time
 192 HONO concentration. We also employ the reaction using the upper limit of the reported uptake
 193 coefficient and calculate the HONO formation rate following Spataro et al. (2013) (Reaction 10).

194

195 VandenBoer et al. (2013) reported that deposited HONO can react with carbonates or soil at night and,
 196 subsequently, be released from the soil during the day by reactions with atmospheric HNO_3 and HCl
 197 (hydrochloric acid). They suggest that this acid displacement process can contribute to a substantial
 198 fraction of day-time HONO. We also use this process (Reactions 11 and 12) and employ a parameter
 199 similar to that of Liu et al. (2019), except that we utilize a displacement efficiency of 6% for HNO_3 and
 200 20% for HCl following VandenBoer et al. (2015).

201

202 Zhou et al., (2003) reported that HNO_3 deposited on environmental surfaces can undergo rapid
 203 photolysis leading to day-time HONO production. Several studies (Sarwar et al., 2008; Fu et al., 2019;
 204 Liu et al., 2019) included such a reaction in their models. However, we do not include it because the
 205 rate constant has high uncertainty and it could also pose a problem for performing long-term model
 206 simulations. For long-term (annual and multiyear) that the deposited amount of HNO_3 could
 207 accumulate with time, which could continue increasing the HONO production rates with time. Soil can
 208 emit HONO and other nitrogen-containing compounds (Su et al., 2011; Oswald et al., 2013). Rasool
 209 et al. (2019) implemented these emissions into CMAQv5.3 by using a mechanistic representation of the
 210 underlying processes and examined their impacts on air quality over North America. The impacts of
 211 HONO emitted from soil are generally low, and we do not include these emissions in this study.

212

213 Table 2 Heterogeneous HONO reactions used in this study

Reaction No.	Reaction	Reaction Rate Constant (k)	Uptake coefficient (γ)	Reference
7a.	$\text{NO}_2 + \text{aerosol} = 0.5 \times \text{HONO} + 0.5 \times \text{HNO}_3$	$k = \frac{1}{4} \gamma v_{\text{NO}_2} \frac{S}{V_a}$	$\gamma_{\text{an}} = 8 \times 10^{-6}$	(Liu et al., 2019)
7b.	$\text{NO}_2 + \text{aerosol} + \text{hv} = 0.5 \times \text{HONO} + 0.5 \times \text{HNO}_3$	$k = \frac{1}{4} \gamma v_{\text{NO}_2} \frac{S}{V_a} \times \frac{J}{J_{\text{max}}}$	$\gamma_{\text{ad}} = 1 \times 10^{-3}$	(Liu et al., 2019)
8a.	$\text{NO}_2 + \text{ground} = \text{HONO}$	$k = \frac{1}{8} \gamma v_{\text{NO}_2} \frac{S}{V_g}$	$\gamma_{\text{gn}} = 4 \times 10^{-6}$	(Li et al., 2018a; Liu et al., 2019)
8b.	$\text{NO}_2 + \text{ground} + \text{hv} = \text{HONO}$	$k = \frac{1}{8} \gamma v_{\text{NO}_2} \frac{S}{V_g} \times \frac{J}{J_{\text{max}}}$	$\gamma_{\text{gd}} = 6 \times 10^{-5}$	(Liu et al., 2019)
9	$\text{NO}_3 + \text{hv} = 0.67 \times \text{HONO} + 0.33 \times \text{NO}_2$	$J = 30 \times J_{\text{HNO}_3}$		(Romer et al., 2018)
10	$\text{NO}_2 + \text{EC} = 0.61 \times \text{HONO} + 0.39 \times \text{NO}$	$k = \frac{1}{4} \gamma v_{\text{NO}_2} \frac{S_{\text{BET}}}{V}$	$\gamma = 2 \times 10^{-6}$	(Spataro and Ianniello, 2014)



11	$\text{HNO}_3 + \text{NaNO}_2 (\text{s}) = \text{HONO} + \text{NaNO}_3 (\text{s})$	$k=0.06V_{\text{dep_HNO}_3}/H$	(VandenBoer et al., 2015)
12	$\text{HCl} + \text{NaNO}_2 (\text{s}) = \text{HONO} + \text{NaCl} (\text{s})$	$k=0.2V_{\text{dep_HCl}}/H$	(VandenBoer et al., 2015)

214 Note:
215 k = first order rate constant (sec^{-1}), γ = heterogeneous uptake coefficient (-), γ_{an} = night-time
216 heterogeneous uptake coefficient on aerosol, γ_{ad} = day-time heterogeneous uptake coefficient on aerosol,
217 γ_{gn} = night-time heterogeneous uptake coefficient on ground, γ_{gd} = day-time heterogeneous uptake
218 coefficient on ground, S/V_{a} = density of aerosol surface; S/V_{g} = density of ground surface; v = mean
219 molecular speed (m/s), HNO_3 = nitric acid, NaNO_2 = sodium nitrite, NaCl = sodium chloride, J = NO_2
220 photolysis rate, J_{max} = maximum NO_2 photolysis rate, $V_{\text{dep_HNO}_3}$ = deposition velocity of HNO_3 (m/s),
221 V_{HCl} = deposition velocity of HCl (m/s), H = the first-layer height (m), and S_{BET}/V = BET surface
222 area-to-volume ratio that we calculate as follows: CMAQv5.3 predicted elemental carbon (EC) ($\mu\text{g}/\text{m}^3$)
223 $\times 1.0 \times 10^{-6}$ ($\text{g}/\mu\text{g}$) $\times 122 \text{ m}^2/\text{g}$, NO_3^- = aerosol nitrate, EC= elemental carbon. Reactions 7a, 7b, 8a, and
224 8b are revised from CMAQv5.3, while reaction numbers 9, 10, 11 and 12 are newly added reactions.

225 2.3 Simulation cases

226 We performed two different simulations using CMAQv5.3 for December 7-22, 2015. One simulation
227 denoted by “ORI” used the gas-phase HONO chemistry in CB6r3 along with the existing
228 heterogeneous hydrolysis of NO_2 in CMAQv5.3. The other simulation denoted by “REV” used the
229 gas-phase HONO chemistry in CB6r3 and the heterogeneous reactions presented in Table 2. For this
230 simulation, we removed the existing heterogeneous hydrolysis of NO_2 in CMAQv5.3. Both simulations
231 used the same HONO emissions (section 2.1). We also completed several additional sensitivity
232 simulations as discussed in Section 3.0.

233
234 We used the ABaCAS national emissions inventory (<http://www.abacas-dss.com>) which resulted in
235 great performance in simulating both NO_2 and fine particle ($\text{PM}_{2.5}$). In previous studies, Zhao et al.
236 (2018) and Zheng et al. (2019) used these emissions and reported a normalized mean bias (NMB) of
237 4% for NO_2 and -17% for $\text{PM}_{2.5}$. Meteorological fields for CMAQv5.3 were simulated using the
238 Weather Research and Forecasting model version 3.8 (WRFv3.8) (Skamarock and Klemp, 2008).
239 WRF has consistent parameterization for cloud fraction simulation, as well as other climate models
240 (see (Xu and Krueger, 1991) and (Xu and Randall, 1996) for a review on this topics). We compared
241 WRF predictions with observed temperature, wind speed, and water vapor mixing ratio in China (Fig.
242 S1). Mean bias (MB) and root mean square error (RMSE) for temperature, wind speed and MB for
243 water vapor mixing ratio meet the benchmark limits suggested by Emery et al.(2001) (Table S1).

244 2.4 Observation data

245 A field campaign was conducted during December 7-22, 2015, at the Research Center for
246 Eco-Environmental Sciences (40.01° N, 116.35° E) to measure atmospheric pollutants and
247 meteorological parameters. Atmospheric concentrations of HONO were measured using a stripping coil
248 (SC) equipped with ion chromatograph (IC). The details of the instrument have been described
249 elsewhere (Xue et al., 2019a). We also completed a statistical analysis of the measurements from the
250 instrument with data from three other methods and concluded that it can provide reliable measurements.



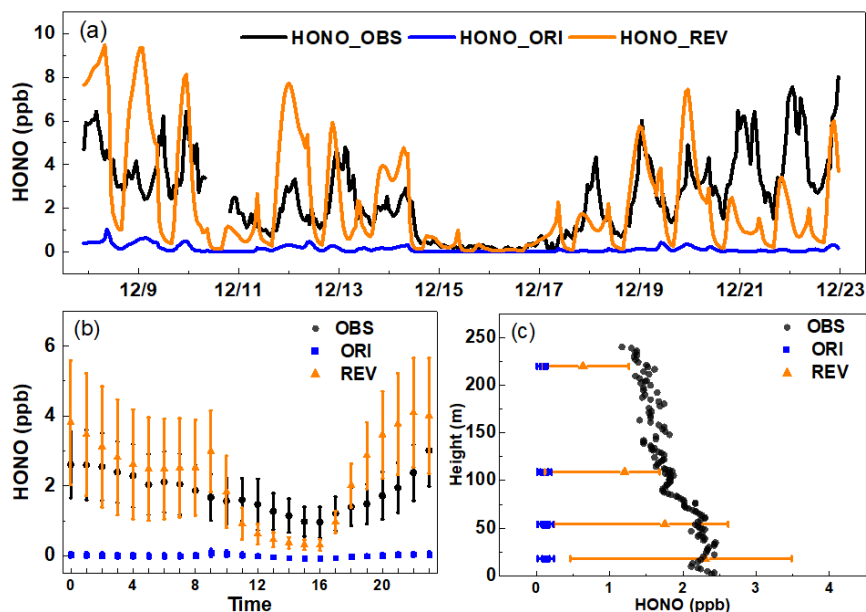
251 The instrument has a minimum detection limit of 4.0 ppt and has been used in several field campaigns
252 (Xue et al., 2019). The concentrations of NO₂ and NO_x were measured by a nitrogen oxide analyzer
253 (Thermo 42i, Thermo Fisher, USA). Sulfur dioxide (SO₂) was measured by a pulsed fluorescence
254 analyzer (Thermo 43i, Thermo Fisher, USA). Fine particles (PM_{2.5}) was measured using an Aerosol
255 Monitor (TSI, Thermo Fisher TEOM 1405). Relative humidity (RH), temperature, wind speed (WS),
256 wind direction (WD), and other metrological data were measured by an automatic weather-monitoring
257 system. Daily atmospheric SO₄²⁻ and NO₃⁻ samples were collected on the roof of a three-story building
258 on the campus of Tsinghua University in Beijing (40.0° N, 116.3° E) and measured by ion
259 chromatography. Details of the measurements method are described by Ma et al. (2020). The hourly
260 averaged concentrations of the main chemical species of PM_{2.5} were measured by the Gas and Aerosol
261 Compositions Monitor (IGAC, Fortelice International Co., Taiwan) monitoring system (Feng et al.,
262 2018). The observed vertical HONO concentrations from the study of Meng et al.(2020) was measured
263 in December of 2016. The OH measurements in January of 2014 were achieved from the study of Tan
264 et al.(2018).
265

266 3 Results and discussions

267 3.1 Comparison of model prediction with observed HONO

268 Observed HONO concentrations vary with time, range between 0.04 ppb to 8 ppb, and contains 11
269 episodes in which the daily peak concentration exceeds 3.3 ppb (Fig. 1a). The high HONO
270 concentration occurs during low wind speeds (Fig. S1). The average HONO concentration during the
271 period is comparable to the reported values for other cities (Table S2). Predicted HONO concentrations
272 obtained with the ORI case are substantially lower than the observed data. In contrast, predicted HONO
273 concentrations obtained with the REV case are substantially higher than those obtained with the ORI
274 case and generally similar to the observed data at night. The ORI case misses the peak values for all
275 episodes, whereas the REV case captures peak values for most episodes. The observed average
276 concentration during the measurement period is 2.5 ppb, the ORI case only predicts an average
277 concentration of 0.1 ppb, whereas the REV case predicts an average concentration of 2.3 ppb. The
278 NMB of HONO is reduced from -96.5% with the ORI case to -4.8% with the REV case.

279
280 Consistent with observations at other cities (Bernard et al., 2015; Fu et al., 2019), the diurnal variation
281 of observed HONO concentrations in Beijing also reveals higher night-time concentrations than
282 day-time values (Fig. 1b). The predictions with ORI case are an order of magnitude lower than the
283 observed diurnal concentrations. The diurnal variation with the REV case shows a remarkable
284 enhancement of night-time HONO concentrations to levels similar to the observed concentrations. It
285 also increases day-time concentrations, however, predicted values are substantially lower than the
286 observed data, which suggests that additional sources are needed to close the gap between observed
287 and predicted day-time HONO concentrations. Night-time and day-time heterogeneous reaction and
288 other updated reactions contribute to the improvement of HONO diurnal pattern. More detailed
289 analysis about this great enhancement is included in section 3.2. The diurnal pattern of the predicted
290 HONO concentrations with the REV agrees better with the observed diurnal pattern.



291

Fig. 1 A comparison of simulated and observed HONO concentrations in Beijing (a) time series (b) diurnal variation, and (c) vertical comparison.

292

293 We compare predicted vertical distribution with observed vertical HONO concentrations (39.97° N,
294 116.38° E) from the study of Meng et al.(2020) (Fig. 1c). The measured concentration is the highest at
295 the surface (2.3 ppb), and concentrations decrease with increasing altitude to a value of ~1.2 ppb at
296 ~200 m, which supports the dominant role of the surface HONO production. Predicted HONO levels
297 with ORI case are too small, whereas predictions with the REV agree better with observed data not
298 only at the surface but also aloft, which provides validity of the simulation results. Consistent with
299 previous HONO vertical concentrations and flux measurements (VandenBoer et al., 2013; Li et al.,
300 2018a), HONO concentration at the surface layer is highest. Model simulated HONO concentrations
301 (Fig. 1c) show a decreasing trend with height similar to the trend in observation data reported by Meng
302 et al.(2020). Model HONO concentrations at upper layers (above 50 m in Fig. 1c) are slightly
303 under-estimated. Model HONO concentrations in these layers are produced mainly by the
304 heterogeneous reaction of NO₂ on aerosol surfaces and the reaction of NO+OH. Aerosol indirect effects
305 can reduce photolysis rate of HONO (Xing et al., 2017). Decreasing photolysis can improve HONO
306 concentrations in the upper layers in polluted air.

307

308 The HONO/NO₂ ratio is used as an indicator to estimate the efficiency of heterogeneous NO₂-HONO
309 conversion (Kleffmann et al., 2006; Li et al., 2012). The observed HONO/NO₂ ratios ranging between
310 0.003 and 0.15 are much higher than reported values in the vehicle exhausts which suggests that
311 HONO formation is governed mainly by the secondary production (Kirchstetter et al., 1996;
312 Kurtenbach et al., 2001). The diurnal variation of observed and predicted HONO/NO₂ ratios are shown
313 in Fig. S2. The predicted HONO/NO₂ ratios increase substantially with REV compared with the ORI
314 case. The average ratio of HONO/NO₂ increases from 0.0027 with ORI and to 0.053 with REV, which



315 is in agreement with the observed value of 0.055. The NMB of hourly average simulated HONO/NO₂
316 ratios at night-time decreases from -94.4% with ORI and to -34.2% with REV. The model results
317 suggest that NO₂ heterogeneous conversion is the most important reaction for simulating atmospheric
318 HONO concentrations.

319
320 According to our detailed literature review in methodology part, uncertainties of HONO prediction
321 might be largely associated with four key parameters and inputs including the uptake coefficient of
322 NO₂ at ground surface, the aerosol nitrate photolysis rates, the daytime photolysis rate, as well as the
323 baseline NO_x emissions. Sensitivity analysis was conducted to examine the influences from those
324 parameters, suggesting that HONO concentration could be doubled with different parameters (see
325 Supplementary Information). Besides, some sources including the photolysis of deposited HNO₃, soil
326 emission and traffic emission could also affect predicted HONO concentration, while the importance of
327 these sources is difficult to quantify. Future studies in improving the accuracy of these parameters are
328 important to reduce the uncertainties of HONO prediction.

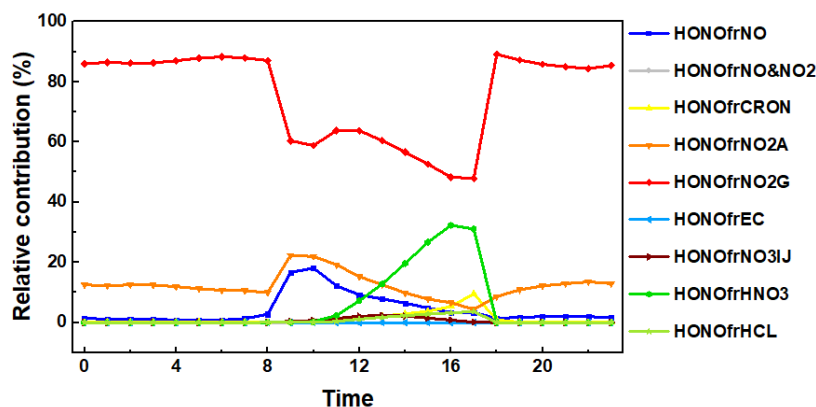
329 3.2 Relative contribution of different HONO reactions

330 To gain insights into HONO reactions, production rates of different reactions are calculated, and the
331 diurnal variation of the production rates is presented in Fig. S5. The production rates from the
332 heterogeneous reaction on ground surfaces (denoted HONOfrNO2G) are higher during the day than
333 those at night because of the higher rate constant. During night-time (18-5 h / 6:00 p.m.-5:00 a.m.), it
334 dominates the HONO production with an average production rate of 1.4 ppb/h. Similar to
335 HONOfrNO2G, the production rates from the heterogeneous reaction on aerosol surfaces (denoted
336 HONOfrNO2A) are also higher during day-time compared with those at night-time. It contributes an
337 average production rate of 0.2 ppb/h during night-time. The contribution of other reactions to
338 night-time HONO production are relatively small (<0.03ppb/h). During day-time (6-17 h / 6:00
339 a.m.-5:00 p.m.), HONOfrNO2G also dominates the production with an average contribution of 2.05
340 ppb/h. HONOfrNO2A is the second most important contributor during day-time with an average
341 production rate of 0.54 ppb/h. The photolysis of NO₃⁻ is the third contributor with an average
342 production of 0.04 ppb/h. Gas-phase reactions collectively contribute an average production rate of
343 ~0.41 ppb/h. The NO+OH reaction is the most important gas-phase reaction, producing HONO at an
344 average rate of 0.37 ppb/h. The average day-time production rates of the acid displacement reactions of
345 HNO₃ and HCl are 0.25 ppb/h and 0.03 ppb/h, respectively. The contribution of the reaction on
346 elemental carbon (EC) is even smaller (<0.01 ppb/h). Day-time production from the heterogeneous
347 reaction on ground and aerosol surfaces is greater than the combined production from all other
348 reactions. Although updated day-time reaction rates are higher than that of night-time, accelerated
349 photochemical loss slow down the HONO increase during day-time.

350
351 The relative contribution of the chemistry updates to HONO formation (REV) is shown in Fig. 2.
352 HONOfrNO2G is the most important reaction, contributing ~86.2% of night-time HONO production.
353 HONOfrNO2A is the second largest contributor, representing ~12.3% of night-time HONO production.
354 During day-time, HONOfrNO2G contributes ~64.7% of the HONO production, whereas
355 HONOfrNO2A is the second largest contributor, representing 12.6% of the HONO production.
356 Day-time HONO production rate from HONOfrNO2A is higher than that at night-time due to the
357 higher rate constant. Consequently, the relative importance of day-time heterogeneous reaction on



358 aerosol surfaces increases, whereas the relative importance of day-time heterogeneous reaction on
359 ground surfaces decreases. The acid displacement reaction of HNO_3 contributes 11% to day-time
360 HONO formation, and its contribution peaks at 5 p.m. (17 h). The average contribution of gas-phase
361 reactions, photolysis of NO_3^- and acid displacement reactions to day-time HONO production are 9.4%,
362 1.0%, and 1.3%, respectively. Note that the reaction of $\text{OH}+\text{NO}$ becomes important in the morning (9
363 to 10 a.m.) during which it contributes 17.4% of the total HONO production. Averaged over the day
364 and night, HONOfrNO2G is the most significant reaction, contributing 75.6% of the HONO production.
365 HONOfrNO2A is the second largest contributor, representing 12.3% of the HONO production. The
366 gas-phase reactions and the acid displacement reaction of HNO_3 are the third most important
367 contributor each accounting for 5.6% of HONO production. Although HONOfrNO2G had a relatively
368 lower uptake coefficient than the aerosol surface reaction, the reaction rate was large because of the
369 greater ground surface area density ($0.047 \text{ m}^2 \text{ m}^{-3}$) compared with the aerosol surface area density
370 ($0.0014 \text{ m}^2 \text{ m}^{-3}$).

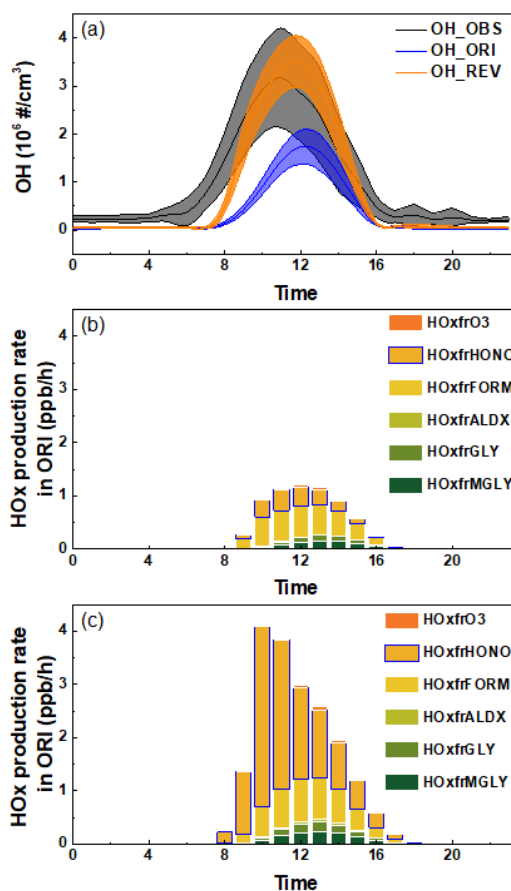


371
372 **Fig. 2** Relative contribution of different HONO reactions to near-ground-level HONO concentration in
373 Beijing in December. The production from the $\text{NO}+\text{OH}$ reaction is denoted as HONOfrNO, the production
374 from the $\text{NO}+\text{NO}_2+\text{H}_2\text{O}$ reaction is denoted as HONOfrNO&NO₂, the production from cresol is denoted as
375 HONOfrCRON, the production from the heterogeneous reaction on ground surfaces is denoted as
376 HONOfrNO₂G, the production from the heterogeneous reaction on aerosol surfaces is denoted as
377 HONOfrNO₂A, the production from the reaction of EC is denoted as HONOfrEC, the production from the
378 photolysis of NO_3^- is denoted as HONOfrNO₃IJ, the production from the acid displacement reaction of HNO_3
379 is denoted as HONOfrHNO₃, and the production from acid displacement reaction of HCl is denoted as
380 HONOfrHCL.

381



382 3.3 Impacts of HONO chemistry on hydroxyl radical concentration



383
384 Fig 3 (a) A comparison of simulated and observed diurnal variation of OH. Shadow in Fig. 3a indicates the
385 range of observation. (b) HO_x formation rates from different photolytic reactions with the ORI case and (c)
386 HO_x formation rates from different photolytic reactions with the REV case. The production of HO_x from the
387 O₃ photolysis is denoted as HOxfrO₃, the production of HO_x from the HONO photolysis is denoted as
388 HOxfrHONO, the production of HO_x from the formaldehyde photolysis is denoted as HOxfrFORM, the
389 production of HO_x from the higher aldehyde photolysis is denoted as HOxfrALDX, the production of HO_x
390 from the glyoxal photolysis is denoted as HOxfrGLY, and the production of HO_x from the methyl glyoxal
391 photolysis is denoted as HOxfrMGLY.

392
393 Enhanced HONO production increases model OH concentration via photolysis. We compare predicted
394 OH concentrations with observed winter data (40.41° N, 116.68° E) reported by Tan et al. (2018) in
395 Fig 3a. Observed concentrations are low ($\sim 2\text{--}3 \times 10^5$ #/cm³) at night and rapidly increase in the morning
396 reaching a peak value of $\sim 3 \times 10^6$ #/cm³ at around 11:00 a.m., then slowly decrease to the low nightly
397 values. The ORI case under-predicts the observed peak value by a factor of ~ 2 , and the model peak
398 time occurs 1 to 1.5 hours after the observed peak time, which is consistent with a previous study in



399 which additional HONO reactions increased OH levels by a factor of >2 (Xue et al., 2020). In addition,
400 the morning enhancement rate with ORI is very low compared with the observed rate. In contrast, the
401 REV case reproduces the observed peak and improves the timing of the peak. The morning
402 enhancement rate also substantially increases and closely tracks the observed enhancement rate. The
403 daily average concentration of OH with REV increases by $\sim 98\%$ compared with that obtained with
404 ORI. Thus, the REV case successfully captures the morning enhancement rate and the peak, and
405 improves the timing of the peak in observed OH data in Beijing. Overall, it captures the observed OH
406 concentration in Beijing much better than the model with the original chemistry. To examine the
407 vertical extent of the impact on OH, predicted OH concentrations with altitude are shown in Fig. S6
408 (40.0° N, 116.3° E). Predicted OH concentration with ORI is the lowest at the surface and increases
409 with altitude primarily because of higher O_3 aloft. The REV case increases OH concentration not only
410 due to the surface HONO but also aloft. However, the impact on OH decreases with altitude as the
411 HONO production decreases with altitude.

412

413 Various photolytic reactions, including the photolysis of O_3 , HONO, formaldehyde, higher aldehyde,
414 glyoxal, and methyl glyoxal, produce HO_x ($OH+HO_2$) are in the model. To understand the relative
415 impacts of these HONO reactions on HO_x production, we compare the diurnal production rates of HO_x
416 from these reactions in Fig. 3b and c. In the ORI case (Fig. 3b), the production of HO_x is relatively
417 small and dominated by the photolysis of HONO and formaldehyde. The photolysis of HONO and
418 formaldehyde start producing HO_x at 9 a.m. which initiates day-time atmospheric chemistry. From late
419 morning, the production of HO_x from glyoxal and methyl glyoxal also contributes to the continuation
420 of day-time atmospheric chemistry. In our simulation, glyoxal and methyl glyoxal originate from the
421 oxidation of aromatics in the atmosphere because isoprene concentration in Beijing is low in winter.
422 Averaged over the entire day, the photolysis of formaldehyde is the largest contributor (0.14 ppb/h) and
423 the photolysis of HONO is the second largest contributor (0.08 ppb/h) to the total HO_x production rate.
424 The production from O_3 and higher aldehyde photolysis are small as their concentrations are low.

425

426 In contrast, the HO_x production rates in the REV case are much higher than those in the ORI case
427 because of the enhanced formation from HONO (Fig. 3c). The photolysis of HONO produces HO_x
428 in the morning, which then kick-starts day-time atmospheric chemistry at 8 a.m. (1 h earlier than in the
429 ORI case) and continues to play an important role during the entire day. From late morning, the
430 production of HO_x from formaldehyde, glyoxal, methyl glyoxal, and higher aldehyde also contributes
431 to the continuation of day-time atmospheric chemistry. The production of HO_x from glyoxal, methyl
432 glyoxal, and higher aldehydes plays a larger role compared with that in the ORI case because of higher
433 concentrations produced by the enhanced oxidation of aromatics by higher OH. The photolysis of
434 HONO is the largest contributor (0.5 ppb/h) to the overall HO_x production rate averaged over the entire
435 day while the photolysis of formaldehyde is the second largest contributor (0.18 ppb/h). Thus, HONO
436 plays a crucial role in producing OH in the morning, without updated reactions, the start of day-time
437 atmospheric chemistry is delayed; and the reaction rates are slower, it also plays an important role in
438 atmospheric chemistry throughout the day. Many other photolytic reactions also produce HO_x in the
439 model; however, the productions from the other pathways are small and do not affect our calculation,
440 hence, they are not shown in the figure.

441

442 HONO can affect greatly the daily OH budget (Harris et al., 1982; Li et al., 2018c; Lu et al., 2019; Xue



443 et al., 2020). Our simulations with the additional HONO reactions enhances OH, which in turn
444 increases HO₂ by the fast conversion between OH and HO₂ radicals (Heard and Pilling, 2003; Lu et al.,
445 2012). The reaction rate of the HO₂+NO reaction increases from 1.8 ppb/h in ORI to 3.6 ppb/h in REV.
446 This indicates that the HONO chemistry also indirectly promotes the formation of OH by increasing
447 the activity of HO₂. This highlights the promoting role of HONO in gas-phase radicals.

448

449 Increased OH concentration oxidizes additional volatile organic compounds (VOCs), lowers the
450 concentrations of precursor species, and increases the concentrations of secondary species (Table S3).
451 Enhanced oxidation of VOCs, sulfur dioxide, and NO₂ leads to secondary pollutants, including SO₄²⁻,
452 NO₃⁻, NH₄⁺, and SOA, which are discussed in the next section.

453 3.4 Impacts of HONO chemistry on the formation of secondary particles

454 Daily averaged model predicted SO₄²⁻, NO₃⁻, and NH₄⁺ concentrations are compared with observed
455 data in Beijing in Fig. 4. The ORI case captures the observed trend but generally under-estimates the
456 observed SO₄²⁻ concentrations, whereas the REV case enhances SO₄²⁻ concentrations and closes the gap
457 between model predictions and observation data. Over the entire simulation period, the average
458 concentration of SO₄²⁻ is increased from 13.3 μg/m³ to 15.8 μg/m³ (19%). CMAQv5.3 includes six
459 chemical pathways for the conversion of SO₂ into SO₄²⁻ (Sarwar et al., 2011). These are ① the
460 gas-phase oxidation of SO₂ by OH, aqueous-phase oxidation of S(IV) (the sum of SO₂•H₂O [hydrated
461 SO₂], HSO₃⁻ [bisulfite ion] and SO₃²⁻ [sulfite ion]) by ② H₂O₂ (hydrogen peroxide), ③ O₃, ④ PAA
462 (peroxyacetic acid), ⑤ MHP (methylhydroperoxide), and ⑥ oxygen catalyzed by the iron (Fe[III])
463 and manganese (Mn[II]). We utilized the sulfate tracking model to examine SO₄²⁻ production from
464 these chemical pathways over Beijing. The SO₄²⁻ production from the gas-phase oxidation of SO₂ by
465 OH in the REV is ~79% greater than that of the ORI case because of the higher OH concentration from
466 HONO photolysis. SO₄²⁻ production from the aqueous-phase oxidation of S(IV) by H₂O₂ in the ORI is
467 relatively small because the predicted H₂O₂ concentration is also small in winter. However, the REV
468 case enhances H₂O₂ concentration, which consequently also increases the SO₄²⁻ production from this
469 pathway. The other chemical pathways produce similar concentrations in both models, except the
470 oxygen catalyzed by the Fe[III] and Mn[II] pathway, which produce slightly lower SO₄²⁻ production in
471 the REV case because of the competition among different chemical pathways and greater oxidation by
472 the OH initiated pathway.

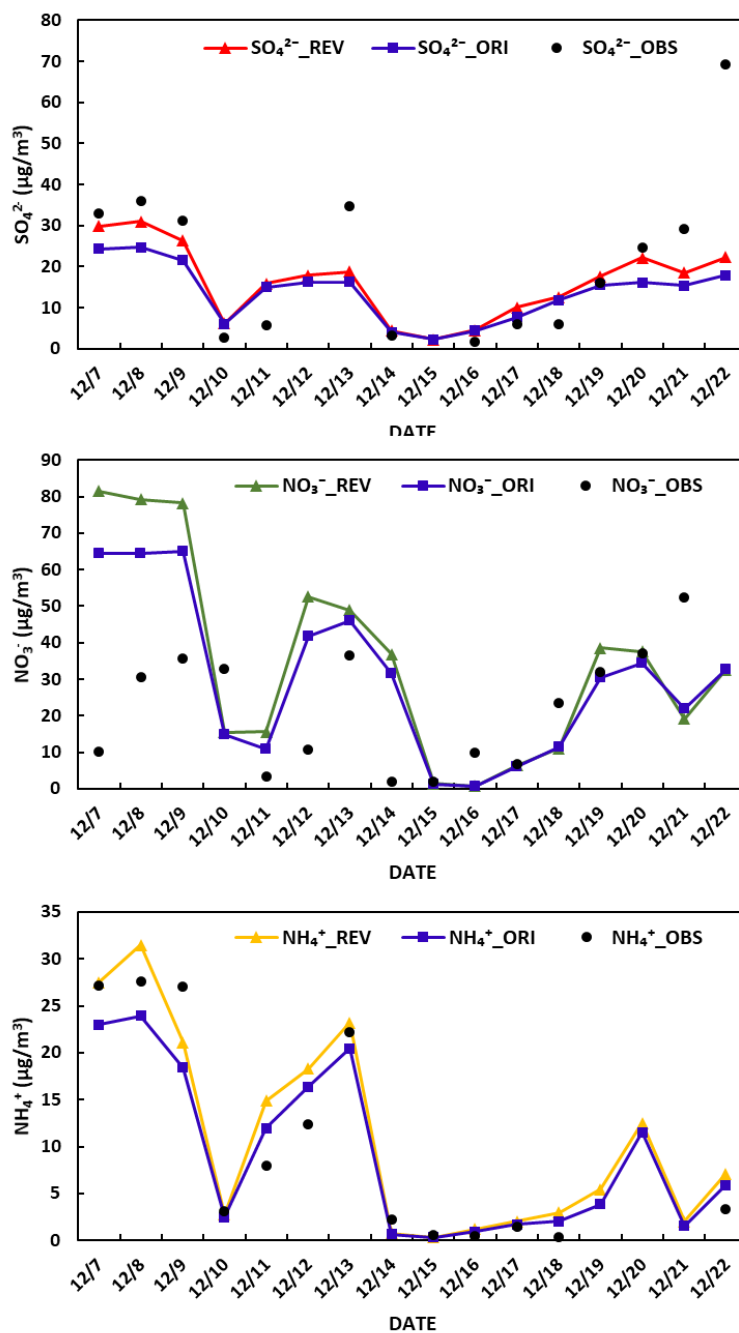
473

474 **Table 3. Predicted SO₄²⁻ concentration in Beijing from different chemical pathways in CMAQv5.3**

Chemical pathway	Average SO ₄ ²⁻ concentration in ORI (μg/m ³)	Average SO ₄ ²⁻ concentration in REV (μg/m ³)
SO ₂ + OH	2.23	3.99
S(IV) + H ₂ O ₂	0.25	0.41
S(IV) + O ₃	0.02	0.02



	S(IV) + O ₂ (TMI)	0.61	0.50
	S(IV) + MHP	0.01	0.01
	S(IV) + PAA	<0.01	<0.01
475	<hr/>		
476	TMI: S(IV) oxidation by oxygen catalyzed by Fe[III] and Mn[II]		



477

478 Fig. 4 A comparison of simulated and observed daily averaged sulfate, nitrate and ammonium concentration
479 in Beijing

480 Additional SO_4^{2-} production is needed in the model to close the gap between the model prediction and



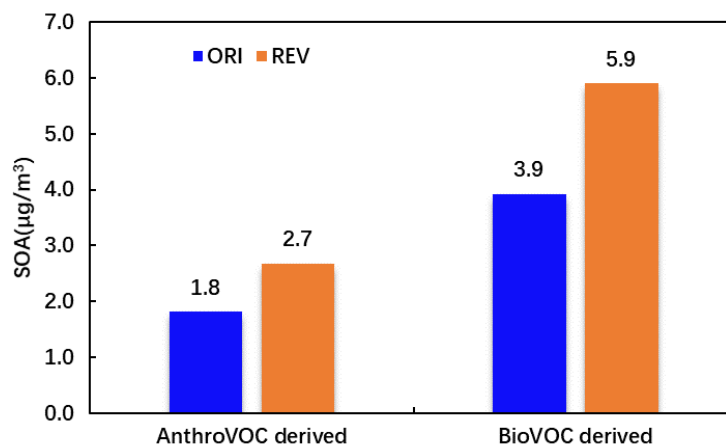
481 observed data. Several investigators have proposed other pathways that can generate additional SO_4^{2-}
482 production. For example, Gen et al. (2019) conducted laboratory experiments and reported that the
483 photolysis of NO_3^- can generate N(III) ($\text{HONO}+\text{NO}_2^-$) in aerosol liquid water, which oxidizes S(IV)
484 into SO_4^{2-} . Zheng et al. (2020) recently incorporated such a pathway and reported that it can enhance
485 SO_4^{2-} production and can explain 15% to 65% of the gap between model predictions and observed
486 SO_4^{2-} concentrations in China. Shao et al. (2019) implemented several additional heterogeneous SO_4^{2-}
487 formation pathways for oxidation of S(IV) in aerosol liquid water and reported that the pathways can
488 enhance SO_4^{2-} production by 20% in China. Wang et al. (2020) recently reported that S(IV) can be
489 oxidized by HONO and NO_2 in cloud and fog to produce SO_4^{2-} in China. Other investigators (Wang et
490 al., 2016; Ye et al., 2018) have suggested additional chemical pathways for SO_4^{2-} production in China.
491 Additional research is needed to further understand the chemical pathways for SO_4^{2-} production in
492 China (Wang et al., 2020b). These pathways are not the focus of this study and, therefore, are not
493 included in our simulations that leads to the model underpredictions. However, our analysis reveals that
494 the HONO chemistry and the subsequent production of OH can enhance SO_4^{2-} production in China, so
495 should be included in air quality models.

496
497 The ORI case has mixed performance in simulating observed NO_3^- (Fig. 4). It over-estimates the
498 daily-averaged observed NO_3^- concentration on some days but captures or under-estimates the observed
499 concentrations on the other. The over-estimation of winter NO_3^- by CMAQ has been reported in
500 previous studies (Yu et al., 2005; Appel et al., 2008). Several reactions contribute to the formation of
501 HNO_3 in CMAQv5.3, which then partitions into NO_3^- . The heterogeneous hydrolysis of N_2O_5 is the
502 most important night-time reaction, and the oxidation of NO_2 by OH is the most important day-time
503 reaction forming HNO_3 . CMAQv5.3 uses the parameterization of Davis et al. (2008) for calculating the
504 uptake coefficient for the heterogeneous hydrolysis of N_2O_5 . It does not include the organic-coating
505 effect (Anttila et al., 2006; Riemer et al., 2009) that can lower the uptake coefficient. Several studies
506 (Brown et al., 2006; Chang et al., 2016; McDuffie et al., 2018; Wang et al., 2020a) have suggested that
507 the parametrizations used in air quality models, including box model, WRF-CHEM and CMAQv5.3,
508 produce higher uptake coefficients than that derived from observation-based studies. These higher
509 uptake coefficients produce high levels of HNO_3 and NO_3^- in the model. A recent study also suggests
510 that the heterogeneous uptake coefficient in China can be even lower than the values derived over the
511 United States (Wang et al., 2020b). Our current model does not include such lower uptake coefficient
512 and over-predicts NO_3^- concentrations. Our IRR analysis of the ORI case results suggests that 30.3% of
513 NO_3^- (averaged over the entire simulation period in Beijing) is produced via night-time heterogeneous
514 hydrolysis of N_2O_5 , and 69.7% is produced via day-time oxidation of NO_2 by OH. The revised
515 chemistry further enhances predicted NO_3^- primarily via the enhanced day-time oxidation of NO_2 .
516 Overall, night-time heterogeneous hydrolysis of N_2O_5 contributes 27.6%, and day-time oxidation of
517 NO_2 contributes 72.4% in the REV case. Consequently, predicted NO_3^- concentrations with the revised
518 chemistry further are overestimated on most days.

519
520 Because of the increased production of SO_4^{2-} and NO_3^- , the average concentration of NH_4^+ also
521 increased from $11.1\mu\text{g}/\text{m}^3$ in ORI and to $13.1\mu\text{g}/\text{m}^3$ in REV (Fig. 4). NH_4^+ formation is promoted by
522 enhancing the neutralization of sulfuric acid and HNO_3 by ammonia. The dissolution of the precursor
523 and the ion balance is the main factor for the growth of NH_4^+ in CMAQv5.3. The overestimation of
524 NO_3^- leads to the overestimation of NH_4^+ (Liu et al., 2020).



525



526

527 **Fig. 5 Predicted monthly average SOA concentration from anthropogenic VOCs (Anthro-VOC-derived) and**
528 **biogenic VOCs (Bio-VOC-derived) in Beijing. Numbers in this figure only involve SOA from representative**
529 **anthropogenic or biogenic VOCs.**

530

531 CMAQv5.3 has a comprehensive treatment of organic aerosols (Murphy et al., 2017; Pye et al., 2017;
532 Xu et al., 2018a), including SOA production from anthropogenic-VOC (Anthro-VOC-derived) and
533 biogenic-VOC (Bio-VOC-derived) Fig. 5 displays the Anthro-VOC-derived and Bio-VOC-derived
534 SOA in Beijing.. The REV case enhances the concentration of Anthro-VOC-derived SOA by $0.9 \mu\text{g}/\text{m}^3$
535 (50%) and Bio -VOC-derived SOA by $2.0 \mu\text{g}/\text{m}^3$ (51%). Enhanced OH from additional HONO
536 enhances the oxidation of VOCs (Table S3) and promotes the SOA formation, which also is reported in
537 previous studies. For example, Xing et al. (2019) used the WRF-CHEM model to examine the impact
538 of HONO chemistry updates on SOA formation over the BTH region in winter and reported that the
539 heterogeneous HONO productions can increase the regional average SOA concentration by 46%.
540 Zhang et al. (2019b) implemented six additional HONO reactions (traffic, soil, biomass burning and
541 indoor emissions, and heterogeneous reactions on aerosol and ground surfaces) in the WRF-CHEM
542 model and reported that it successfully reproduced the observed HONO concentrations in Wangdu.
543 They suggested that the additional HONO reactions can increase 2 to $15 \mu\text{g}/\text{m}^3$ of SOA
544 (meridional-mean) in the BTH region on heavy haze days.

545

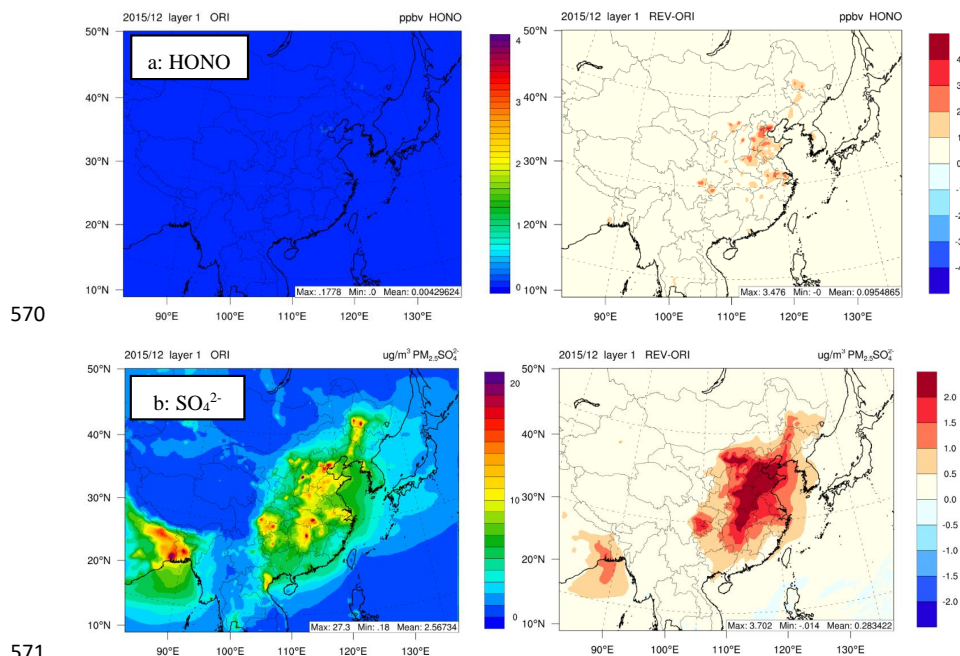
546 3.5 Spatial impacts on selected species

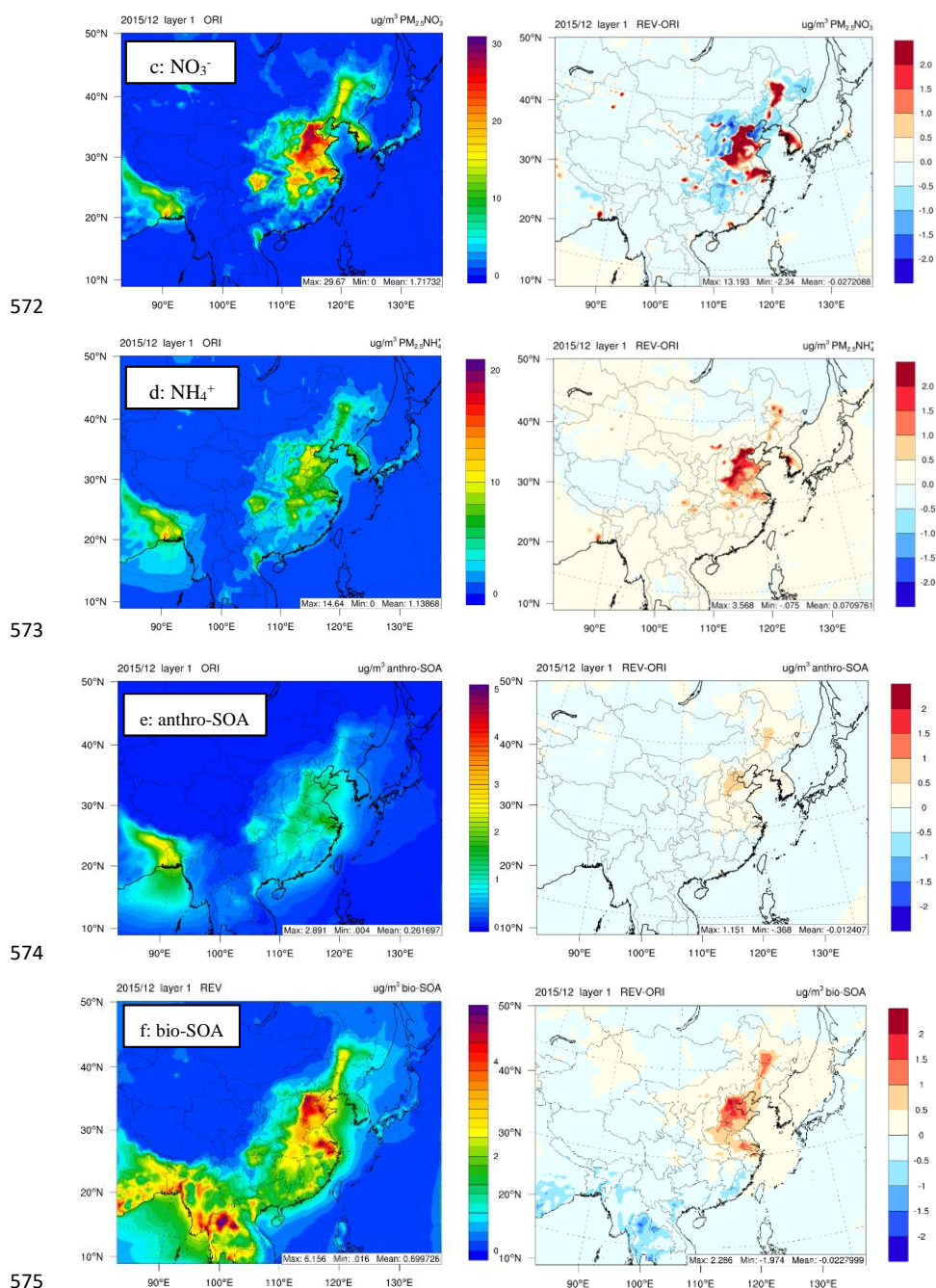
547 We examine the spatial impacts of the revised HONO chemistry on selected species (HONO, SO_4^{2-} ,
548 NO_3^- , NH_4^+ , and SOA) in Fig. 6. Predicted average HONO concentrations with ORI are low (<0.18 ppb)
549 over the entire modeling domain. The revised chemistry increases HONO concentrations over the
550 North China Plain (i.e., BTH, Henan, Shandong) by 0.5 to 3.0 ppb. Abundant emissions of NO_x in this
551 area results in higher NO_2 concentrations, which subsequently enhance HONO concentrations, as the
552 NO_2 reaction on ground is the dominated HONO production source (Fig. 2). It also increases HONO in
553 some other urban areas; however, the impacts in most other areas are relatively small. The ORI case



554 predicts higher average SO_4^{2-} , NO_3^- , and NH_4^+ concentrations over the North China Plain and the
555 northeast cities. The revised chemistry enhances average of SO_4^{2-} by 1 to 3 $\mu\text{g}/\text{m}^3$, with the maximum
556 enhancements over the south part of the Hebei province. It increases NO_3^- by up to 1.5 $\mu\text{g}/\text{m}^3$ and NH_4^+
557 by up to 1.1 $\mu\text{g}/\text{m}^3$ over the North China Plain. It also slightly decreases NO_3^- over the North China
558 Plain. The revised HONO chemistry decreases NO_2 concentration while increasing OH concentration.
559 Thus, day-time production of HNO_3 from the NO_2+OH pathway depends on the relative magnitude of
560 the changes of the reaction rate and tends to increase the production in high- NO_x areas while
561 decreasing it in low- NO_x areas. HNO_3 partitions into NO_3^- ; thus, changes in HNO_3 production leads to
562 changes in NO_3^- concentration. The ORI case predicts the highest anthropogenic SOA (anthro-SOA)
563 and biogenic SOA (bio-SOA) concentrations over northeast China and the North China Plain. The
564 revised model increases anthro-SOA by 0.37 to 1.2 $\mu\text{g}/\text{m}^3$ over this area and changes bio-SOA over the
565 North China Plain and the northeast cities by -2.0 to 2.3 $\mu\text{g}/\text{m}^3$. Isoprene emissions in some southern
566 cities are relatively higher than in cities in North China Plain in the model. Glyoxal and methylglyoxal
567 generated from isoprene are oxidized by increased OH from the HONO chemistry. SOA derived from
568 biogenic VOC, therefore, is reduced in some areas in Guangdong.

569





576
577 **Fig. 6** Spatial distributions of monthly averaged (a) HONO, (b) sulfate, (c) nitrate, (d) ammonium, (e)
578 anthro-VOC-derived SOA, (f) and bio-VOC-derived SOA concentrations simulated with ORI and the
579 differences (REV-ORI) between the two simulations in December 2015.



580 4 Summary

581 The existing HONO chemistry in CMAQv5.3 cannot re-produce the observed winter HONO
582 concentrations in Beijing. Thus, we revised the HONO chemistry in CMAQv5.3 by implementing
583 several heterogeneous HONO formation pathways. Model predictions with the revised chemistry
584 generally agree with observed HONO concentrations, although the model cannot predict the higher
585 observed day-time concentrations. The heterogeneous production on ground accounts for nearly 75%
586 of the total HONO production. Enhanced HONO increases day-time OH concentrations, which also
587 agree well with observed data in Beijing. Predicted OH concentrations with the existing HONO
588 chemistry are lower than observed data almost by a factor of two. The morning OH enhancement rate is
589 lower than the observed rate, and the timing of the peak is delayed. The revised HONO chemistry
590 improves the morning OH enhancement rate and reproduces the daily peak and the timing of the daily
591 peak. Enhanced OH increases the oxidation rates of SO₂, NO₂, and VOCs in the atmosphere and
592 produces additional secondary pollutants. The revised HONO chemistry moderately enhances SO₄²⁻
593 concentration in this study. The impact of HONO chemistry on SO₄²⁻ concentration is likely to be
594 greater than shown in this article. For example, HONO chemistry enhances NO₃⁻, which, in turn, can
595 produce additional SO₄²⁻ via the photolysis of NO₃⁻ (Zheng et al., 2020). The oxidation of S(IV) by
596 HONO in cloud and fog also can produce additional SO₄²⁻ (Wang et al., 2020). Such pathways are not
597 the focus of this study and are not included in the current model. A recent study (Chen et al., 2019)
598 suggests that HONO also can form on snow-covered ground, which can potentially affect wintertime
599 air quality. Thus, a future study incorporating such chemical reactions to comprehensively examine the
600 impact of HONO chemistry on air quality in different seasons and geographical areas is envisioned.

601
602

603 Acknowledgements

604 This work was financially supported by the National Natural Science Foundation of China (41877304,
605 41907190, 51861135102), and the Youth Innovation Promotion Association, CAS (2018060). This
606 work was also financially and technically supported by Toyota Motor Corporation and Toyota Central
607 Research and Development Laboratories Inc. This work was completed on the “Explorer 100” cluster
608 system of Tsinghua National Laboratory for Information Science and Technology.

609

610 Disclaimer

611 The views expressed in this paper are those of the authors and do not necessarily represent the views or
612 policies of the U.S. EPA.

613

614 Reference

- 615 An, J., Li, Y., Chen, Y., Li, J., Qu, Y., Tang, Y., 2012. Enhancements of major aerosol components due
616 to additional HONO sources in the North China Plain and implications for visibility and haze.
617 *Advances in Atmospheric Sciences* 30, 57-66.
- 618 Anttila, T., Kiendler-Scharr, A., Tillmann, R., Mentel, T.F., 2006. On the Reactive Uptake of Gaseous



- 619 Compounds by Organic-Coated Aqueous Aerosols: Theoretical Analysis and Application to the
620 Heterogeneous Hydrolysis of N₂O₅. *The Journal of Physical Chemistry A* 110, 10435-10443.
- 621 Appel, W., Bhawe, P., Gilliland, A., Sarwar, G., Roselle, S., 2008. Evaluation of the community
622 multiscale air quality (CMAQ) model version 4.5: Sensitivities impacting model performance; Part II -
623 particulate matter. *Atmospheric Environment* 42, 6057-6066.
- 624 Bao, F.X., Li, M., Zhang, Y., Chen, C.C., Zhao, J.C., 2018. Photochemical Aging of Beijing Urban
625 PM_{2.5}: HONO Production. *Environmental Science & Technology* 52, 6309-6316.
- 626 Bernard, F., Cazaunau, M., Gosselin, B., Zhou, B., Zheng, J., Liang, P., Zhang, Y., Ye, X., Daële, V.,
627 Mu, Y., Zhang, R., Chen, J.-M., Mellouki, A., 2015. Measurements of nitrous acid (HONO) in urban
628 area of Shanghai, China. *Environmental Science and Pollution Research* 23.
- 629 Brown, S.S., Ryerson, T.B., Wollny, A.G., Brock, C.A., Peltier, R., Sullivan, A.P., Weber, R.J., Dubé,
630 W.P., Trainer, M., Meagher, J.F., Fehsenfeld, F.C., Ravishankara, A.R., 2006. Variability in Nocturnal
631 Nitrogen Oxide Processing and Its Role in Regional Air Quality. *Science* 311, 67.
- 632 Byun, D., Schere, K.L., 2006. Review of the governing equations, computational algorithms, and other
633 components of the Models-3 Community Multiscale Air Quality (CMAQ) modeling system. *Applied*
634 *mechanics reviews* 59, 51-77.
- 635 Chang, W.L., Brown, S.S., Stutz, J., Middlebrook, A.M., Bahreini, R., Wagner, N.L., Dubé, W.P.,
636 Pollack, I.B., Ryerson, T.B., Riemer, N., 2016. Evaluating N₂O₅ heterogeneous hydrolysis
637 parameterizations for CalNex 2010. *Journal of Geophysical Research: Atmospheres* 121, 5051-5070.
- 638 Chen, Q., Edebeli, J., McNamara, S.M., Kulju, K.D., May, N.W., Bertman, S.B., Thanekar, S., Fuentes,
639 J.D., Pratt, K.A., 2019. HONO, Particulate Nitrite, and Snow Nitrite at a Midlatitude Urban Site during
640 Wintertime. *ACS Earth and Space Chemistry* 3, 811-822.
- 641 Cui, L.L., Li, R., Zhang, Y.C., Meng, Y., Fu, H.B., Chen, J.M., 2018. An observational study of nitrous
642 acid (HONO) in Shanghai, China: The aerosol impact on HONO formation during the haze episodes.
643 *Sci. Total Environ.* 630, 1057-1070.
- 644 Czader, B.H., Li, X., Rappenglueck, B., 2013. CMAQ modeling and analysis of radicals, radical
645 precursors, and chemical transformations. *Journal of Geophysical Research: Atmospheres* 118,
646 11,376-311,387.
- 647 Czader, B.H., Rappenglück, B., Percell, P., Byun, D.W., Ngan, F., Kim, S., 2012. Modeling nitrous acid
648 and its impact on ozone and hydroxyl radical during the Texas Air Quality Study 2006. *Atmospheric*



- 649 Chemistry and Physics 12, 6939-6951.
- 650 Davis, J.M., Bhawe, P.V., Foley, K.M., 2008. Parameterization of N_2O_5
- 651 reaction probabilities on the surface of particles containing ammonium, sulfate, and nitrate. Atmos.
- 652 Chem. Phys. 8, 5295-5311.
- 653 Emery, A.E., Muntoni, F., Quinlivan, R.C., 2015. Duchenne muscular dystrophy. OUP Oxford.
- 654 Emery, C., Tai, E., 2001. Enhanced Meteorological Modeling and Performance Evaluation for Two
- 655 Texas Ozone Episodes.
- 656 Feng, T., Bei, N.F., Zhao, S.Y., Wu, J.R., Li, X., Zhang, T., Cao, J.J., Zhou, W.J., Li, G.H., 2018.
- 657 Wintertime nitrate formation during haze days in the Guanzhong basin, China: A case study.
- 658 Environmental pollution 243, 1057-1067.
- 659 Fu, X., Wang, T., Zhang, L., Li, Q.Y., Wang, Z., Xia, M., Yun, H., Wang, W.H., Yu, C., Yue, D.L., Zhou,
- 660 Y., Zheng, J.Y., Han, R., 2019. The significant contribution of HONO to secondary pollutants during a
- 661 severe winter pollution event in southern China. Atmospheric Chemistry and Physics 19, 1-14.
- 662 Gen, M., Zhang, R., Huang, D.D., Li, Y., Chan, C.K., 2019. Heterogeneous SO_2 Oxidation in Sulfate
- 663 Formation by Photolysis of Particulate Nitrate. Environmental Science & Technology Letters 6, 86-91.
- 664 Guo, S., Hu, M., Zamora, M.L., Peng, J., Shang, D., Zheng, J., Du, Z., Wu, Z., Shao, M., Zeng, L.,
- 665 Molina, M.J., Zhang, R., 2014. Elucidating severe urban haze formation in China. Proceedings of the
- 666 National Academy of Sciences 111, 17373-17378.
- 667 Harris, G.W., Carter, W.P.L., Winer, A.M., Pitts, J.N., Platt, U., Perner, D., 1982. Observations of
- 668 nitrous acid in the Los Angeles atmosphere and implications for predictions of ozone-precursor
- 669 relationships. Environmental Science & Technology 16, 414-419.
- 670 He, H., Wang, Y., Ma, Q., Ma, J., Chu, B., Ji, D., Tang, G., Liu, C., Zhang, H., Hao, J., 2014. Mineral
- 671 dust and NO_x promote the conversion of SO_2 to sulfate in heavy pollution days. Scientific Reports 4.
- 672 Heard, D.E., Pilling, M.J., 2003. Measurement of OH and HO_2 in the Troposphere. Chemical reviews
- 673 103, 5163-5198.
- 674 Huang, L., Zhao, Y., Li, H., Chen, Z., 2015. Kinetics of Heterogeneous Reaction of Sulfur Dioxide on
- 675 Authentic Mineral Dust: Effects of Relative Humidity and Hydrogen Peroxide. Environmental Science
- 676 & Technology 49, 10797-10805.
- 677 Huang, R.-J., Zhang, Y., Bozzetti, C., Ho, K.-F., Cao, J.-J., Han, Y., Daellenbach, K.R., Slowik, J.G.,
- 678 Platt, S.M., Canonaco, F., 2014. High secondary aerosol contribution to particulate pollution during



- 679 haze events in China. *Nature* 514, 218-222.
- 680 Karamchandani, P., Emery, C., Yarwood, G., Lefer, B., Stutz, J., Couzo, E., Vizuete, W., 2015.
- 681 Implementation and refinement of a surface model for heterogeneous HONO formation in a 3-D
- 682 chemical transport model. *Atmospheric Environment* 112, 356-368.
- 683 Kirchstetter, T.W., Harley, R.A., Littlejohn, D., 1996. Measurement of nitrous acid in motor vehicle
- 684 exhaust. *Environmental science & technology* 30, 2843-2849.
- 685 Kleffmann, J., Gavriloiiei, T., Hofzumahaus, A., Holland, F., Koppmann, R., Rupp, L., Schlosser, E.,
- 686 Siese, M., Wahner, A., 2005. Daytime formation of nitrous acid: A major source of OH radicals in a
- 687 forest. *Geophysical Research Letters* 32.
- 688 Kleffmann, J., Lörzer, J., Wiesen, P., Kern, C., Trick, S., Volkamer, R., Rodenas, M., Wirtz, K., 2006.
- 689 Intercomparison of the DOAS and LOPAP techniques for the detection of nitrous acid (HONO).
- 690 *Atmospheric Environment* 40, 3640-3652.
- 691 Kulmala, M., 2018. Build a global Earth observatory. *Nature* 553, 21-23.
- 692 Kurtenbach, R., Becker, K., Gomes, J., Kleffmann, J., Lörzer, J., Spittler, M., Wiesen, P., Ackermann,
- 693 R., Geyer, A., Platt, U., 2001. Investigations of emissions and heterogeneous formation of HONO in a
- 694 road traffic tunnel. *Atmospheric Environment* 35, 3385-3394.
- 695 Lelieveld, J., Evans, J.S., Fnais, M., Giannadaki, D., Pozzer, A., 2015. The contribution of outdoor air
- 696 pollution sources to premature mortality on a global scale. *Nature* 525, 367-371.
- 697 Li, D.D., Xue, L.K., Wen, L., Wang, X.F., Chen, T.S., Mellouki, A., Chen, J.M., Wang, W.X., 2018a.
- 698 Characteristics and sources of nitrous acid in an urban atmosphere of northern China: Results from 1-yr
- 699 continuous observations. *Atmospheric Environment* 182, 296-306.
- 700 Li, G., Bei, N., Cao, J., Huang, R., Wu, J., Feng, T., Wang, Y., Liu, S., Zhang, Q., Tie, X., Molina, L.T.,
- 701 2017. A possible pathway for rapid growth of sulfate during haze days in China. *Atmospheric*
- 702 *Chemistry and Physics* 17, 3301-3316.
- 703 Li, G., Lei, W., Zavala, M., Volkamer, R., Dusanter, S., Stevens, P., Molina, L.T., 2010. Impacts of
- 704 HONO sources on the photochemistry in Mexico City during the MCMA-2006/MILAGO Campaign.
- 705 *Atmos. Chem. Phys.* 10, 6551-6567.
- 706 Li, L., Duan, Z., Li, H., Zhu, C., Henkelman, G., Francisco, J.S., Zeng, X.C., 2018b. Formation of
- 707 HONO from the NH₃-promoted hydrolysis of NO₂ dimers in the atmosphere. *Proceedings of the*
- 708 *National Academy of Sciences of the United States of America* 115, 7236-7241.



- 709 Li, L.J., Hoffmann, M.R., Colussi, A.J., 2018c. Role of Nitrogen Dioxide in the Production of Sulfate
710 during Chinese Haze-Aerosol Episodes. *Environmental Science & Technology* 52, 2686-2693.
- 711 Li, M., Su, H., Li, G., Ma, N., Pöschl, U., Cheng, Y., 2019. Relative importance of gas uptake on
712 aerosol and ground surfaces characterized by equivalent uptake coefficients. *Atmospheric Chemistry
713 and Physics* 19, 10981-11011.
- 714 Li, X., Brauers, T., Häseler, R., Bohn, B., Fuchs, H., Hofzumahaus, A., Holland, F., Lou, S., Lu, K.D.,
715 Rohrer, F., Hu, M., Zeng, L.M., Zhang, Y.H., Garland, R.M., Su, H., Nowak, A., Wiedensohler, A.,
716 Takegawa, N., Shao, M., Wahner, A., 2012. Exploring the atmospheric chemistry of nitrous acid
717 (HONO) at a rural site in Southern China. *Atmospheric Chemistry and Physics* 12, 1497-1513.
- 718 Liu, Y., Lu, K., Li, X., Dong, H., Tan, Z., Wang, H., Zou, Q., Wu, Y., Zeng, L., Hu, M., Min, K.-E.,
719 Kecorius, S., Wiedensohler, A., Zhang, Y., 2019. A Comprehensive Model Test of the HONO Sources
720 Constrained to Field Measurements at Rural North China Plain. *Environmental Science & Technology*
721 53, 3517-3525.
- 722 Liu, Y., Zhang, Y., Lian, C., Yan, C., Feng, Z., Zheng, F., Fan, X., Chen, Y., Wang, W., Chu, B., Wang,
723 Y., Cai, J., Du, W., Daellenbach, K.R., Kangasluoma, J., Bianchi, F., Kujansuu, J., Petäjä, T., Wang, X.,
724 Hu, B., Wang, Y., Ge, M., He, H., Kulmala, M., 2020. The promotion effect of nitrous acid on aerosol
725 formation in wintertime Beijing: possible contribution of traffic-related emission. *Atmospheric
726 Chemistry and Physics Discussions* 2020, 1-43.
- 727 Liu, Z., Wang, Y., Costabile, F., Amoroso, A., Zhao, C., Huey, L.G., Stickel, R., Liao, J., Zhu, T., 2014.
728 Evidence of Aerosols as a Media for Rapid Daytime HONO Production over China. *Environmental
729 Science & Technology* 48, 14386-14391.
- 730 Lu, K., Fuchs, H., Hofzumahaus, A., Tan, Z., Wang, H., Zhang, L., Schmitt, S.H., Rohrer, F., Bohn, B.,
731 Broch, S., Dong, H., Gkatzelis, G.I., Hohaus, T., Holland, F., Li, X., Liu, Y., Liu, Y., Ma, X., Novelli, A.,
732 Schlag, P., Shao, M., Wu, Y., Wu, Z., Zeng, L., Hu, M., Kiendler-Scharr, A., Wahner, A., Zhang, Y.,
733 2019. Fast Photochemistry in Wintertime Haze: Consequences for Pollution Mitigation Strategies.
734 *Environmental Science & Technology* 53, 10676-10684.
- 735 Lu, K.D., Rohrer, F., Holland, F., Fuchs, H., Bohn, B., Brauers, T., Chang, C.C., Häseler, R., Hu, M.,
736 Kita, K., Kondo, Y., Li, X., Lou, S.R., Nehr, S., Shao, M., Zeng, L.M., Wahner, A., Zhang, Y.H.,
737 Hofzumahaus, A., 2012. Observation and modelling of OH and HO₂ concentrations in the Pearl River Delta 2006: a missing OH source in a VOC rich atmosphere.



- 739 Atmospheric Chemistry and Physics 12, 1541-1569.
- 740 Lu, X.C., Wang, Y.H., Li, J.F., Shen, L., Fung, J.C.H., 2018. Evidence of heterogeneous HONO
741 formation from aerosols and the regional photochemical impact of this HONO source. Environ. Res.
742 Lett. 13, 12.
- 743 Ma, T., Furutani, H., Duan, F., Kimoto, T., Jiang, J., Zhang, Q., Xu, X., Wang, Y., Gao, J., Geng, G., Li,
744 M., Song, S., Ma, Y., Che, F., Wang, J., Zhu, L., Huang, T., Toyoda, M., He, K., 2020. Contribution of
745 hydroxymethanesulfonate (HMS) to severe winter haze in the North China Plain. Atmos. Chem. Phys.
746 Discuss. 2020, 1-17.
- 747 Mathur, R., Roselle, S., Pouliot, G., Sarwar, G., 2008. Diagnostic analysis of the three-dimensional
748 sulfur distributions over the eastern United states using the CMAQ model and measurements from the
749 ICARTT field experiment, Air Pollution Modeling and Its Application XIX. Springer, pp. 496-504.
- 750 McDuffie, E.E., Fibiger, D.L., Dubé, W.P., Lopez-Hilfiker, F., Lee, B.H., Thornton, J.A., Shah, V.,
751 Jaeglé, L., Guo, H., Weber, R.J., Michael Reeves, J., Weinheimer, A.J., Schroder, J.C., Campuzano-Jost,
752 P., Jimenez, J.L., Dibb, J.E., Veres, P., Ebben, C., Sparks, T.L., Wooldridge, P.J., Cohen, R.C.,
753 Hornbrook, R.S., Apel, E.C., Campos, T., Hall, S.R., Ullmann, K., Brown, S.S., 2018. Heterogeneous
754 N₂O₅ Uptake During Winter: Aircraft Measurements During the 2015 WINTER Campaign and
755 Critical Evaluation of Current Parameterizations. Journal of Geophysical Research: Atmospheres 123,
756 4345-4372.
- 757 Meng, F., Qin, M., Tang, K., Duan, J., Fang, W., Liang, S., Ye, K., Xie, P., Sun, Y., Xie, C., Ye, C., Fu,
758 P., Liu, J., Liu, W., 2020. High-resolution vertical distribution and sources of HONO and
759 NO₂ in the nocturnal boundary layer in urban Beijing, China. Atmospheric
760 Chemistry and Physics 20, 5071-5092.
- 761 Monge, M., D'Anna, B., Mazri, L., Giroir-Fendler, A., Ammann, M., Donaldson, D.J., George, C.,
762 2010. Light changes the atmospheric reactivity of soot. Proceedings of the National Academy of
763 Sciences of the United States of America 107, 6605-6609.
- 764 Murphy, B.N., Woody, M.C., Jimenez, J.L., Carlton, A.M.G., Hayes, P.L., Liu, S., Ng, N.L., Russell,
765 L.M., Setyan, A., Xu, L., Young, J., Zaveri, R.A., Zhang, Q., Pye, H.O.T., 2017. Semivolatile POA and
766 parameterized total combustion SOA in CMAQv5.2: impacts on source strength and partitioning.
767 Atmos. Chem. Phys. 17, 11107-11133.
- 768 Oswald, R., Behrendt, T., Ermel, M., Wu, D., Su, H., Cheng, Y., Breuninger, C., Moravek, A., Mougín,



- 769 E., Delon, C., 2013. HONO emissions from soil bacteria as a major source of atmospheric reactive
770 nitrogen. *Science* 341, 1233-1235.
- 771 Pye, H.O.T., Murphy, B.N., Xu, L., Ng, N.L., Carlton, A.G., Guo, H., Weber, R., Vasilakos, P., Appel,
772 K.W., Budisulistiorini, S.H., Surratt, J.D., Nenes, A., Hu, W., Jimenez, J.L., Isaacman-VanWertz, G.,
773 Misztal, P.K., Goldstein, A.H., 2017. On the implications of aerosol liquid water and phase separation
774 for organic aerosol mass. *Atmos. Chem. Phys.* 17, 343-369.
- 775 Quan, J., Tie, X., Zhang, Q., Liu, Q., Li, X., Gao, Y., Zhao, D., 2014. Characteristics of heavy aerosol
776 pollution during the 2012–2013 winter in Beijing, China. *Atmospheric Environment* 88, 83-89.
- 777 Rasool, Q.Z., Bash, J.O., Cohan, D.S., 2019. Mechanistic representation of soil nitrogen emissions in
778 the Community Multiscale Air Quality (CMAQ) model v 5.1. *Geosci Model Dev* 12, 849-878.
- 779 Riemer, N., Vogel, H., Vogel, B., Anttila, T., Kiendler-Scharr, A., Mentel, T.F., 2009. Relative
780 importance of organic coatings for the heterogeneous hydrolysis of N₂O₅ during summer in Europe.
781 *Journal of Geophysical Research: Atmospheres* 114.
- 782 Romer, P.S., Wooldridge, P.J., Crounse, J.D., Kim, M.J., Wennberg, P.O., Dibb, J.E., Scheuer, E., Blake,
783 D.R., Meinardi, S., Brosius, A.L., Thames, A.B., Miller, D.O., Brune, W.H., Hall, S.R., Ryerson, T.B.,
784 Cohen, R.C., 2018. Constraints on Aerosol Nitrate Photolysis as a Potential Source of HONO and NO_x.
785 *Environmental Science & Technology* 52, 13738-13746.
- 786 Sarwar, G., Fahey, K., Napelenok, S., Roselle, S., Mathur, R., 2011. Examining the impact of CMAQ
787 model updates on aerosol sulfate predictions, The 10th Annual CMAS Models-3 User's Conference,
788 October, Chapel Hill, NC.
- 789 Sarwar, G., Roselle, S.J., Mathur, R., Appel, W., Dennis, R.L., Vogel, B., 2008. A comparison of
790 CMAQ HONO predictions with observations from the northeast oxidant and particle study.
791 *Atmospheric Environment* 42, 5760-5770.
- 792 Shao, J., Chen, Q., Wang, Y., Lu, X., He, P., Sun, Y., Shah, V., Martin, R.V., Philip, S., Song, S., Zhao,
793 Y., Xie, Z., Zhang, L., Alexander, B., 2019. Heterogeneous sulfate aerosol formation mechanisms
794 during wintertime Chinese haze events: air quality model assessment using observations of sulfate
795 oxygen isotopes in Beijing. *Atmos. Chem. Phys.* 19, 6107-6123.
- 796 Skamarock, W.C., Klemp, J.B., 2008. A time-split nonhydrostatic atmospheric model for weather
797 research and forecasting applications. *Journal of computational physics* 227, 3465-3485.
- 798 Spataro, F., Ianniello, A., 2014. Sources of atmospheric nitrous acid: State of the science, current



799 research needs, and future prospects. *J. Air Waste Manage. Assoc.* 64, 1232-1250.

800 Spataro, F., Ianniello, A., Esposito, G., Allegrini, I., Zhu, T., Hu, M., 2013. Occurrence of atmospheric
801 nitrous acid in the urban area of Beijing (China). *Sci. Total Environ.* 447, 210-224.

802 Stemmler, K., Ammann, M., Donders, C., Kleffmann, J., George, C., 2006. Photosensitized reduction
803 of nitrogen dioxide on humic acid as a source of nitrous acid. *Nature* 440, 195-198.

804 Stutz, J., Alicke, B., Neftel, A., 2002. Nitrous acid formation in the urban atmosphere: Gradient
805 measurements of NO₂ and HONO over grass in Milan, Italy. *Journal of Geophysical Research:*
806 *Atmospheres* 107, LOP 5-1-LOP 5-15.

807 Su, H., Cheng, Y., Oswald, R., Behrendt, T., Trebs, I., Meixner, F.X., Andreae, M.O., Cheng, P., Zhang,
808 Y., Pöschl, U., 2011. Soil Nitrite as a Source of Atmospheric HONO and OH Radicals. *Science* 333,
809 1616.

810 Sun, Y., Wang, Z., Fu, P., Jiang, Q., Yang, T., Li, J., Ge, X., 2013. The impact of relative humidity on
811 aerosol composition and evolution processes during wintertime in Beijing, China. *Atmospheric*
812 *Environment* 77, 927-934.

813 Tan, Z., Rohrer, F., Lu, K., Ma, X., Bohn, B., Broch, S., Dong, H., Fuchs, H., Gkatzelis, G.I.,
814 Hofzumahaus, A., Holland, F., Li, X., Liu, Y., Liu, Y., Novelli, A., Shao, M., Wang, H., Wu, Y., Zeng,
815 L., Hu, M., Kiendler-Scharr, A., Wahner, A., Zhang, Y., 2018. Wintertime photochemistry in Beijing:
816 observations of RO_x radical concentrations in the North China Plain during the BEST-ONE campaign.
817 *Atmos. Chem. Phys.* 18, 12391-12411.

818 Tong, S., Hou, S., Zhang, Y., Chu, B., Liu, Y., He, H., Zhao, P., Ge, M., 2016. Exploring the nitrous
819 acid (HONO) formation mechanism in winter Beijing: direct emissions and heterogeneous production
820 in urban and suburban areas. *Faraday discussions* 189, 213-230.

821 Tsona, N.T., Du, L., 2019. A potential source of atmospheric sulfate from O₂-induced SO₂ oxidation
822 by ozone. *Atmos. Chem. Phys.* 19, 649-661.

823 VandenBoer, T.C., Brown, S.S., Murphy, J.G., Keene, W.C., Young, C.J., Pszenny, A.A.P., Kim, S.,
824 Warneke, C., de Gouw, J.A., Maben, J.R., Wagner, N.L., Riedel, T.P., Thornton, J.A., Wolfe, D.E.,
825 Dubé, W.P., Öztürk, F., Brock, C.A., Grossberg, N., Lefer, B., Lerner, B., Middlebrook, A.M., Roberts,
826 J.M., 2013. Understanding the role of the ground surface in HONO vertical structure: High resolution
827 vertical profiles during NACHTT-11. *Journal of Geophysical Research: Atmospheres* 118,
828 10,155-110,171.



- 829 VandenBoer, T.C., Young, C.J., Talukdar, R.K., Markovic, M.Z., Brown, S.S., Roberts, J.M., Murphy,
830 J.G., 2015. Nocturnal loss and daytime source of nitrous acid through reactive uptake and displacement.
831 *Nature Geoscience* 8, 55-60.
- 832 Wang, G., Cheng, S., Wei, W., Yang, X., Wang, X., Jia, J., Lang, J., Lv, Z., 2017. Characteristics and
833 emission-reduction measures evaluation of PM_{2.5} during the two major events: APEC and Parade. *The*
834 *Science of the total environment* 595, 81-92.
- 835 Wang, G., Zhang, R., Gomez, M.E., Yang, L., Levy Zamora, M., Hu, M., Lin, Y., Peng, J., Guo, S.,
836 Meng, J., Li, J., Cheng, C., Hu, T., Ren, Y., Wang, Y., Gao, J., Cao, J., An, Z., Zhou, W., Li, G., Wang,
837 J., Tian, P., Marrero-Ortiz, W., Secretst, J., Du, Z., Zheng, J., Shang, D., Zeng, L., Shao, M., Wang, W.,
838 Huang, Y., Wang, Y., Zhu, Y., Li, Y., Hu, J., Pan, B., Cai, L., Cheng, Y., Ji, Y., Zhang, F., Rosenfeld, D.,
839 Liss, P.S., Duce, R.A., Kolb, C.E., Molina, M.J., 2016. Persistent sulfate formation from London Fog to
840 Chinese haze. *Proceedings of the National Academy of Sciences of the United States of America*.
- 841 Wang, H., Chen, X., Lu, K., Tan, Z., Ma, X., Wu, Z., Li, X., Liu, Y., Shang, D., Wu, Y., Zeng, L., Hu,
842 M., Schmitt, S., Kiendler-Scharr, A., Wahner, A., Zhang, Y., 2020a. Wintertime N₂O₅ uptake
843 coefficients over the North China Plain. *Science Bulletin* 65, 765-774.
- 844 Wang, J., Li, J., Ye, J., Zhao, J., Wu, Y., Hu, J., Liu, D., Nie, D., Shen, F., Huang, X., Huang, D.D., Ji,
845 D., Sun, X., Xu, W., Guo, J., Song, S., Qin, Y., Liu, P., Turner, J.R., Lee, H.C., Hwang, S., Liao, H.,
846 Martin, S.T., Zhang, Q., Chen, M., Sun, Y., Ge, X., Jacob, D.J., 2020b. Fast sulfate formation from
847 oxidation of SO₂ by NO₂ and HONO observed in Beijing haze. *Nature Communications* 11, 2844.
- 848 Wang, L.W., Wen, L., Xu, C.H., Chen, J.M., Wang, X.F., Yang, L.X., Wang, W.X., Yang, X., Sui, X.,
849 Yao, L., Zhang, Q.Z., 2015. HONO and its potential source particulate nitrite at an urban site in North
850 China during the cold season. *Sci. Total Environ.* 538, 93-101.
- 851 Xing, J., Mathur, R., Pleim, J., Hogrefe, C., Gan, C.M., Wong, D.C., Wei, C., Wang, J.D., 2015. Air
852 pollution and climate response to aerosol direct radiative effects: A modeling study of decadal trends
853 across the northern hemisphere. *J. Geophys. Res.-Atmos.* 120, 16.
- 854 Xing, J., Wang, J., Mathur, R., Wang, S., Sarwar, G., Pleim, J., Hogrefe, C., Zhang, Y., Jiang, J., Wong,
855 D.C., Hao, J., 2017. Impacts of aerosol direct effects on tropospheric ozone through changes in
856 atmospheric dynamics and photolysis rates. *Atmospheric Chemistry and Physics* 17, 9869-9883.
- 857 Xing, L., Wu, J., Elser, M., Tong, S., Liu, S., Li, X., Liu, L., Cao, J., Zhou, J., El-Haddad, I., Huang, R.,
858 Ge, M., Tie, X., Prévôt, A.S.H., Li, G., 2019. Wintertime secondary organic aerosol formation in



- 859 Beijing–Tianjin–Hebei (BTH): contributions of HONO sources and heterogeneous reactions. *Atmos.*
860 *Chem. Phys.* 19, 2343-2359.
- 861 Xu, K.-M., Krueger, S.K., 1991. Evaluation of Cloudiness Parameterizations Using a Cumulus
862 Ensemble Model. *Monthly Weather Review* 119, 342-367.
- 863 Xu, K.-M., Randall, D.A., 1996. Evaluation of Statistically Based Cloudiness Parameterizations Used
864 in Climate Models. *Journal of Atmospheric Sciences* 53, 3103-3119.
- 865 Xu, L., Pye, H.O.T., He, J., Chen, Y., Murphy, B.N., Ng, N.L., 2018a. Experimental and model
866 estimates of the contributions from biogenic monoterpenes and sesquiterpenes to secondary organic
867 aerosol in the southeastern United States. *Atmos. Chem. Phys.* 18, 12613-12637.
- 868 Xu, W., Kuang, Y., Zhao, C., Tao, J., Zhao, G., Bian, Y., Yu, Y., Shen, C., Liang, L., Zhang, G., 2018b.
869 NH₃ promoted hydrolysis of NO₂ induces explosive growth in HONO. *Atmospheric Chemistry and*
870 *Physics Discussions*, 1-22.
- 871 Xue, C., Ye, C., Ma, Z., Liu, P., Zhang, Y., Zhang, C., Tang, K., Zhang, W., Zhao, X., Wang, Y., Song,
872 M., Liu, J., Duan, J., Qin, M., Tong, S., Ge, M., Mu, Y., 2019. Development of stripping coil-ion
873 chromatograph method and intercomparison with CEAS and LOPAP to measure atmospheric HONO.
874 *Sci. Total Environ.* 646, 187-195.
- 875 Xue, C., Zhang, C., Ye, C., Liu, P., Catoire, V., Krysztofiak, G., Chen, H., Ren, Y., Zhao, X., Wang, J.,
876 Zhang, F., Zhang, C., Zhang, J., An, J., Wang, T., Chen, J., Kleffmann, J., Mellouki, A., Mu, Y., 2020.
877 HONO budget and its role in nitrate formation in the rural North China Plain. *Environmental Science*
878 *& Technology*.
- 879 Ye, C., Gao, H., Zhang, N., Zhou, X., 2016. Photolysis of Nitric Acid and Nitrate on Natural and
880 Artificial Surfaces. *Environmental Science & Technology* 50, 3530-3536.
- 881 Ye, C., Liu, P., Ma, Z., Xue, C., Zhang, C., Zhang, Y., Liu, J., Liu, C., Sun, X., Mu, Y., 2018. High
882 H₂O₂ concentrations observed during haze periods during the winter in Beijing: Importance of H₂O₂
883 oxidation in sulfate formation. *Environmental Science & Technology Letters* 5, 757-763.
- 884 Ye, C., Zhang, N., Gao, H., Zhou, X., 2017. Photolysis of Particulate Nitrate as a Source of HONO and
885 NO_x. *Environmental Science & Technology* 51, 6849-6856.
- 886 Yu, S., Dennis, R., Roselle, S., Nenes, A., Walker, J., Eder, B., Schere, K., Swall, J., Robarge, W., 2005.
887 An assessment of the ability of three-dimensional air quality models with current thermodynamic
888 equilibrium models to predict aerosol NO₃⁻. *Journal of Geophysical Research* 110.



889 Zhang, J., Chen, J., Xue, C., Chen, H., Zhang, Q., Liu, X., Mu, Y., Guo, Y., Wang, D., Chen, Y., Li, J.,
890 Qu, Y., An, J., 2019a. Impacts of six potential HONO sources on HOx budgets and SOA formation
891 during a wintertime heavy haze period in the North China Plain. *Sci. Total Environ.* 681, 110-123.
892 Zhang, J.W., An, J.L., Qu, Y., Liu, X.G., Chen, Y., 2019b. Impacts of potential HONO sources on the
893 concentrations of oxidants and secondary organic aerosols in the Beijing-Tianjin-Hebei region of China.
894 *Sci. Total Environ.* 647, 836-852.
895 Zhang, S., Xing, J., Sarwar, G., Ge, Y., He, H., Duan, F., Zhao, Y., He, K., Zhu, L., Chu, B., 2019c.
896 Parameterization of heterogeneous reaction of SO₂ to sulfate on dust with coexistence of NH₃ and
897 NO₂ under different humidity conditions. *Atmospheric Environment* 208, 133-140.
898 Zhang, W.Q., Tong, S.R., Ge, M.F., An, J.L., Shi, Z.B., Hou, S.Q., Xia, K.H., Qu, Y., Zhang, H.X., Chu,
899 B.W., Sun, Y.L., He, H., 2019d. Variations and sources of nitrous acid (HONO) during a severe
900 pollution episode in Beijing in winter 2016. *Sci. Total Environ.* 648, 253-262.
901 Zhao, B., Zheng, H., Wang, S., Smith, K.R., Lu, X., Aunan, K., Gu, Y., Wang, Y., Ding, D., Xing, J., Fu,
902 X., Yang, X., Liou, K.-N., Hao, J., 2018. Change in household fuels dominates the decrease in
903 PM_{2.5} exposure and premature mortality in China in 2005–2015. *Proceedings*
904 *of the National Academy of Sciences* 115, 12401.
905 Zheng, B., Zhang, Q., Zhang, Y., He, K.B., Wang, K., Zheng, G.J., Duan, F.K., Ma, Y.L., Kimoto, T.,
906 2015. Heterogeneous chemistry: a mechanism missing in current models to explain secondary
907 inorganic aerosol formation during the January 2013 haze episode in North China. *Atmospheric*
908 *Chemistry and Physics* 15, 2031-2049.
909 Zheng, H., Zhao, B., Wang, S., Wang, T., Ding, D., Chang, X., Liu, K., Xing, J., Dong, Z., Aunan, K.,
910 Liu, T., Wu, X., Zhang, S., Wu, Y., 2019. Transition in source contributions of PM_{2.5} exposure and
911 associated premature mortality in China during 2005–2015. *Environment International* 132, 105111.
912 Zhou, X., Gao, H., He, Y., Huang, G., Bertman, S.B., Civerolo, K., Schwab, J., 2003. Nitric acid
913 photolysis on surfaces in low-NO_x environments: Significant atmospheric implications. *Geophysical*
914 *Research Letters* 30.
915
916 U.S. Environmental Protection Agency (EPA), Office of Research and Development (ORD): CMAQ
917 (Version 5.3), Zenodo, <https://doi.org/10.5281/zenodo.3379043>, Washington, DC, USA, August 2019.
918